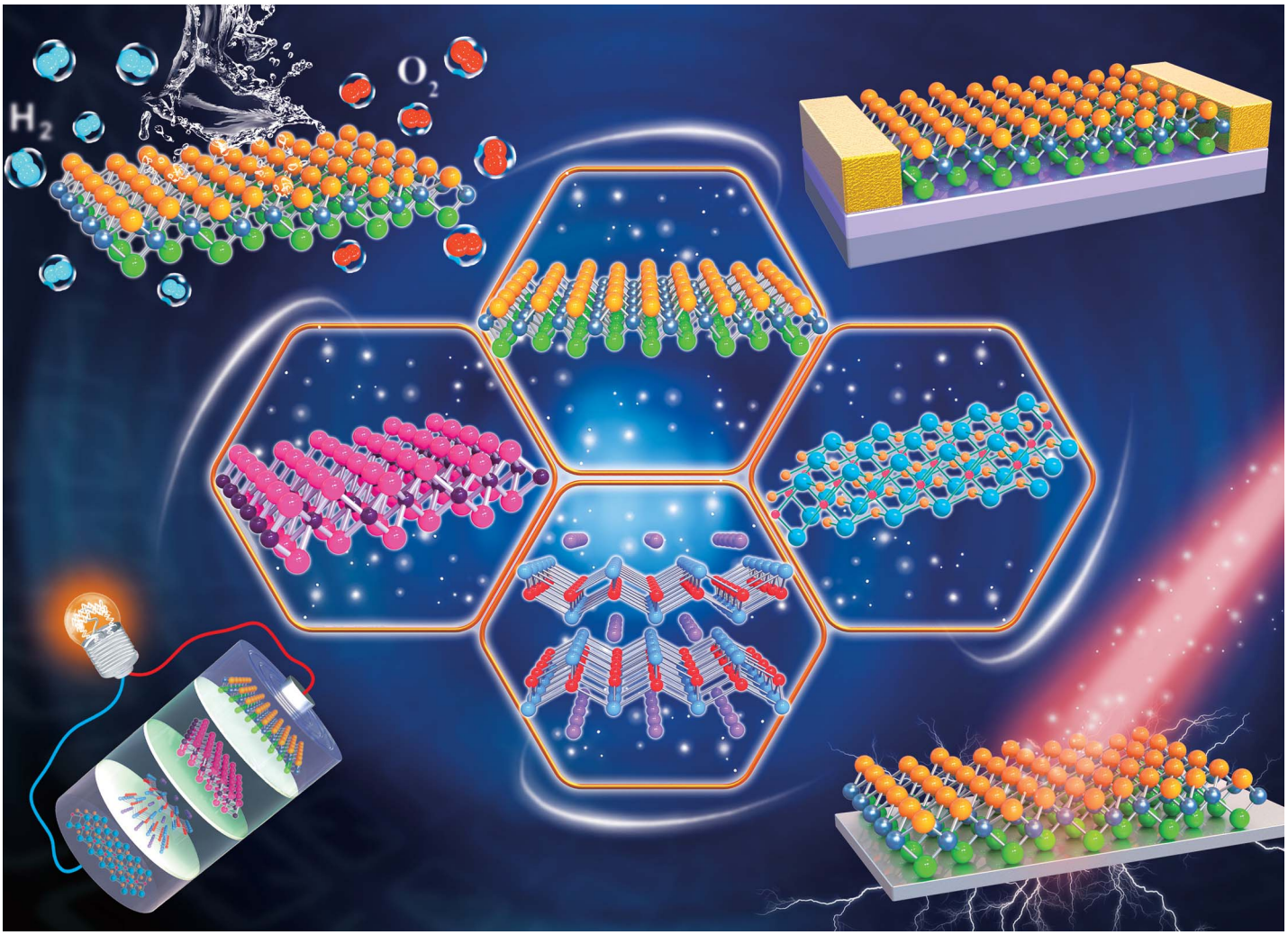

Showcasing a review on recent advances of ternary 2D materials by Dr Peng Hu and Prof. Zheng Liu at the Nanyang Technological University and Assoc. Prof. Xuexia He at Shaanxi Normal University.

Recent advances in ternary two-dimensional materials: synthesis, properties and applications

The synthesis, structure, characterization, physical properties and applications of different kinds of ternary 2D materials are systematically summarized and further discussed.

As featured in:

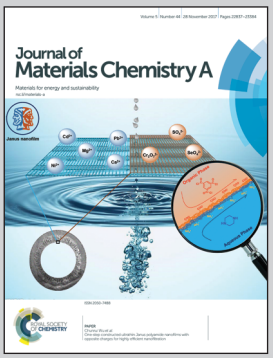

See Peng Hu, Zheng Liu, Xuexia He *et al.*, *J. Mater. Chem. A*, 2017, **5**, 22855.

ROYAL SOCIETY OF CHEMISTRY

rsc.li/materials-a

Registered charity number: 207890

Journal of Materials Chemistry A

REVIEW

View Article Online
View Journal | View Issue

Cite this: J. Mater. Chem. A, 2017, 5, 22855

Recent advances in ternary two-dimensional materials: synthesis, properties and applications

Lina Wang,[ab] Peng Hu,*[c] Yi Long,[c] Zheng Liu *[cd] and Xuexia He*[ab]

Received 8th August 2017
Accepted 2nd October 2017

DOI: 10.1039/c7ta06971e

rsc.li/materials-a

Two-dimensional (2D) materials have gained significant attention owing to their unique physical and chemical properties, which arise mainly from their high surface–bulk ratios and topological effects. Since the discovery of graphene in 2004, the family of 2D materials has expanded rapidly. Thus far, several single-element 2D materials (graphene, phosphorene, *etc.*) have been reported; the majority of them contain two (MoS_2, WSe_2, *etc.*) or more elements (Mo_2CT_x, $CrPS_4$, $Bi_2Sr_2CaCu_2O_x$, *etc.*). Of these, three-element 2D materials, also called ternary 2D materials, represent a rather attractive direction of recent years. Typical ternary 2D materials include metal phosphorous trichalcogenides (MPTs), ternary transition metal chalcogenides (TMDs), transition metal carbides and nitrides (MXenes) and 2D ternary oxides. Ternary 2D systems result in multiple degrees of freedom to tailor their physical properties *via* stoichiometric variation. Moreover, they exhibit some properties not characteristic of binary 2D systems, such as band gap tuning. In this paper, we have reviewed the recent progress in various ternary 2D materials on the basis of their classification (MPTs, ternary 2D MXenes, ternary TMDs, BCN and other ternary 2D materials). The synthesis methods, structures, key properties (such as band gap tuning, phase transition and topological phase), and their applications, are summarized. In addition, the strategies to tackle challenges, as well as the outlooks of this field, are presented.

1 Introduction

Since the discovery of graphene in 2004,[1] atomically thin two-dimensional (2D) materials have attracted considerable interest owing to their unprecedented physical, chemical and electronic properties.[2] They have shown great potential in various applications in electronic and optoelectronic devices, catalysis, sensors and energy storage devices.[3–11] Prompted by the increasing research on graphene, researchers have started to explore and

[a]Key Laboratory of Applied Surface and Colloid Chemistry, Shaanxi Normal University, Ministry of Education, Xi'an 710062, PR China. E-mail: xxhe@snnu.edu.cn
[b]Shaanxi Engineering Lab for Advanced Energy Technology, School of Materials Science and Engineering, Shaanxi Normal University, Xi'an 710119, China
[c]School of Materials Science and Engineering, Nanyang Technological University, 639798, Singapore. E-mail: phu003@e.ntu.edu.sg
[d]School of Electrical and Electronic Engineering, Nanyang Technological University, 639798, Singapore. E-mail: Z.Liu@ntu.edu.sg

Lina Wang received her B.S. degree from Shanxi Normal University. Currently she is a master student in the School of Materials Science & Engineering at Shaanxi Normal University under the supervision of Associate Prof. Xuexia He. Her research interests mainly focus on the design and synthesis of ternary 2D materials.

Peng Hu obtained his B.S. (2006) and M.S. (2009) degrees in chemistry from Shaanxi Normal University, and completed his Ph.D. (under the guidance of Professor Christian Kloc) in materials science at Nanyang Technological University, Singapore from 2012 to 2016. He is now a research fellow at Nanyang Technological University, Singapore. His current research interests focus on the single crystal growth of organics, low dimensional materials and organic–inorganic hybrids, and their electronic and optoelectronic applications.

isolate other layered materials. After decades of progress, various 2D materials have been reported, including MoS_2, h-BN, WTe_2, germylene and black phosphorus.[12–19] Note that the physical, chemical and electronic properties of 2D materials are versatile and material-dependent, making each of them favorable for specific applications.[13,14,20] For example, the structure of h-BN is similar to that of graphene. However, unlike graphene, h-BN is an insulator, with a band gap larger than 5 eV. The band gap of single-layered h-BN could be up to 6 eV. Most importantly, h-BN is resistant to chemical attack and harsh conditions such as high temperature.[14,21,22] Therefore, the exploration of new 2D materials with interesting novel properties is crucial for building the landscape of the 2D world thus leading to fascinating applications.

Currently, research on 2D materials has been almost exclusively focused on single elements, such as graphene and black phosphorus and on binary systems such as MoS_2 and WS_2. A majority of the 2D materials are binary systems.[14,15] In addition, efforts have been devoted to the discovery of new 2D materials, to meet the requirements of future electronic and optoelectronic technologies. Therefore, 2D materials with multiple elements, such as Mo_2CT_x, $CrPS_4$ and $Bi_2Sr_2CaCu_2O_x$, have also been reported recently.[23,24] Among these, three-element 2D materials, also called ternary 2D materials, represent a rather attractive research direction. Typical ternary 2D materials include metal phosphorous trichalcogenides (MPT: $MnPS_3$, $CrPS_4$, $FePSe_3$, *etc.*), ternary transition metal carbides, carbonitrides and nitrides (MXenes: Ta_6AlC_5 and Ti_7SnC_6), and ternary transition metal dichalcogenides (TMDs: $Mo_xW_{2-x}S_2$, $Cr_2Ge_2Te_6$ and so on).[13,14,25,26] Previous studies have shown that the elemental composition plays an important role in determining the physical properties of 2D materials. For example, the typical single-element 2D material graphene has charge carrier mobility but no band gap. Another new single-element 2D material antimonene becomes a semiconductor when it is thinned to a single layer. However, the number of elementary 2D materials is rather limited.

In contrast, binary systems exhibit a relatively diversiform behavior because of their large number of compounds. Good candidates can be easily identified for diverse applications. For example, an indirect band gap can be transformed into a direct band gap by layering the samples. The 1T–2H phase transition in transition metal dichalcogenides (such as $MoTe_2$) can be controlled by the growth temperature. Binary 2D materials exhibit excellent flexibility for tuning the properties through stoichiometry engineering.[27–30] However, it is difficult to tune the bang gap in most binary 2D materials.[31,32] More importantly, the band gaps of these 2D materials are usually too large to make appropriate optical devices. Although binary InSe was reported to have a relatively narrow band gap of 1.4 eV,[33] its application in the near infrared (NIR) range is difficult. However, some TMDs, which have a very narrow band gap, might be very good for NIR detectors. In this case, a ternary 2D system may provide a solution to the above mentioned problems.[25,34] Further, bulk ternary tritellurides $CrATe_3$ (A = Si and Ge) were predicted to have

Yi Long is a Senior Lecturer in the School of Materials Science and Engineering at Nanyang Technological University, Singapore. She obtained her Ph.D. degree from the University of Cambridge, UK. Her research focuses on nanostructured functional materials. She has successfully implemented technology transfer from lab to industry, and is now serving as a principal investigator in various research programs relating to functional coatings.

Zheng Liu was born in Hubei, China in 1983. He received his B.Sc. (2005) and Ph.D (2010) in physics from the National Center for Nanoscience and Technology (NCNST), China, under the guidance of Professor Lianfeng Sun. He then worked in Prof. Pulickel M. Ajayan's and Prof. Jun Lou's groups as a joint postdoc research fellow and research scientist at Rice University (USA). Currently, he is Nanyang Assistant Professor at Nanyang Technological University, Singapore. His research focuses on the growth, characterization and performance of large-scale and high-quality novel low-dimensional crystals and their hybridized architectures, as well as their applications in high-performance electronics, optical devices and energy conversion and storage.

Xuexia He received her Ph.D. in 2013 from Okayama University, Japan, under the guidance of Professor Yoshihiro Kubozono. Then she joined Assistant Professor Zheng Liu's groups as a research fellow at Nanyang Technological University, Singapore. Now she is an Associate Professor in the School of Materials Science and Engineering of Shaanxi Normal University, China. Currently, her research interests focus on 2D materials for rechargeable Li-ion batteries and photoelectric detectors.

a small band gap of 0.04 and 0.06 eV, respectively.[35] In copper–indium–selenium systems, the band gap energies of $CuIn_3Se_5$ (1.17 eV) and $CuIn_5Se_8$ (1.22–1.24 eV) are larger than that of chalcopyrite-type $CuInSe_2$ (0.99 eV). Importantly, they exhibit a variety of structures depending on the ratio of Cu, In and Se, including chalcopyrite, stannite and wurtzite structures. The crystal structure of the samples changed from chalcopyrite-type $CuInSe_2$ to hexagonal $CuIn_5Se_8$ through stannite-type $CuIn_3Se_5$ with increasing x (decreasing Cu/In ratio).[34]

Similar to the ternary copper indium selenide system, ternary 2D systems have multiple degrees of freedom for tailoring their physical properties *via* stoichiometric variation.[23] Further, ternary systems exhibit some properties that are not shown in binary 2D systems. For example, binary 2D materials include metals and semiconductors with exceptionally strong light–matter coupling,[36] charge density wave and superconducting order.[37–40] One strategy to search theoretically for magnetism in 2D materials is to explore the magnetic properties of the single layers exfoliated from a bulk material that exhibits a robust magnetic order.[41] As such, layered ternary 2D systems are an ideal platform for this line of research. $MnPX_3$ ternary chalcogenides are predicted to have strain-tunable ferromagnetic phases.[26,42–44] For larger atomic number compounds such as $CrGeTe_3$ and $CrSnTe_3$, the density functional theory (DFT) predicts ferromagnetic semiconducting phases with Curie temperatures of 80–170 K.[26,45] The CrGeTe system is a particularly interesting material since it is in a highly rare class of ferromagnetic semiconductors and possesses a layered structure because of the van der Waals bonds. The van der Waals bonds make it a candidate 2D atomic crystal, which is predicted as a platform for the study of 2D semiconducting ferromagnets and for single-layered spintronic devices. Spin–phonon coupling can be a key factor for spin relaxation in spintronic devices. Such coupling has also been confirmed in the CrGeTe system.[46]

Ternary 2D systems not only exhibit outstanding physical, chemical and electronic properties but also have additional unique properties that binary 2D systems do not possess. In this case, the investigation of ternary 2D systems is of great significance. Fig. 1 summarizes the classification, physical properties and potential applications of ternary 2D materials. In this review, the synthesis of ternary TMDs, MPTs, ternary MXenes and other ternary 2D materials is systematically summarized in Section 2, including chemical vapor deposition (CVD), chemical vapor transport (CVT) and molecular beam epitaxy (MBE). In the third section, the structure and characterization of these ternary 2D materials are introduced. Then, the physical properties, including band gap tuning, phase transition and the topological phase are discussed in Section 4. Furthermore, the potential applications, such as in energy, catalysis and devices are presented. The last section presents the future prospects and a summary of the review.

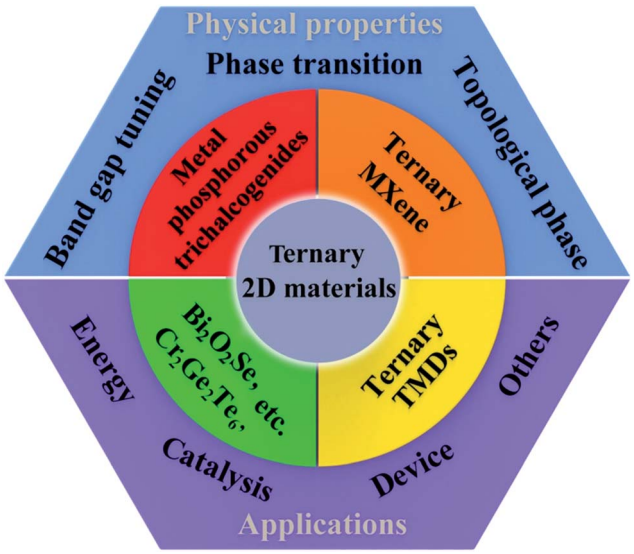

Fig. 1 Schematic representation summarizing the classification, physical properties and applications of ternary 2D materials.

2 Synthesis

2.1 Ternary TMDs

Researchers have confirmed that, compared to BCN, some representative ternary TMDs have no phase separation. Moreover, such ternary TMDs have been predicted to be relatively stable owing to their low mixing free energy.[47] CVD is one of the most commonly used methods to obtain ternary TMDs. Shifa *et al.* devised a rational method to synthesize pure ternary $Co_xW_{(1-x)}S_2$ nanosheets by transferring Co from CoO/carbon fiber (CF) nanowires to the already formed WS_2/W foil nanosheets. In this experiment, for the first time, Co was incorporated into a WS_2 nanosheet without any concomitant side phases.[48] Another study reported, for the first time, a one-step CVD strategy for the growth of high-quality ternary alloy $Mo_{(1-x)}W_xS_2$ monolayers on SiO_2/Si substrates with controllable composition. The $Mo_{(1-x)}W_xS_2$ and $MoS_{2(1-x)}Se_{2x}$ alloys, both with excellent uniformity and controllable compositions, were synthesized in this study.[51]

In another study, a single-crystal monolayer $Mo_xW_{1-x}S_2$ alloy heterostructure with an in-plane inhomogeneous composition was fabricated using the conventional CVD method.[52] Gong *et al.* reported a one-step direct synthesis of $MoS_{2(1-x)}Se_{2x}$ atomic mono- and bilayers with a broad range of selenium concentrations on SiO_2 by CVD (Fig. 2a).[49]

Another method of preparing ternary TMDs is the CVT approach. For instance, $WS_{2(1-x)}Se_{2x}$ ($x = 0.5$) crystals have been synthesized by using the CVT method.[53] Konkena *et al.* produced MoSSe@r-GO composite materials, in which MoSSe was synthesized by CVT, followed by a liquid exfoliation process.[54] In addition, ZrS_xSe_{2-x}, which is a layered n-type TMD semiconductor with an indirect band gap, has been obtained by this method.[55] Further, a new ternary phase ZrSTe in the form of a single crystal has been successfully grown from pure elements by using the CVT technique with iodine as the transport agent.[56]

Ternary TMDs can be obtained easily by exfoliation, including mechanical and electrochemical exfoliation. Łapińska reported the Raman measurements of $PbSnS_2$ thin films obtained by the mechanical exfoliation of a single crystal.[57] Yu *et al.* studied the $WSe_{2(1-x)}Te_{2x}$ monolayer

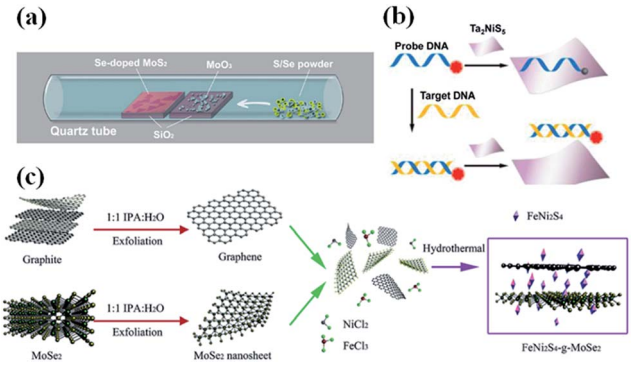

Fig. 2 Methods for preparing ternary TMDs. (a) Controlled synthesis of $MoS_{2(1-x)}Se_{2x}$ layers *via* CVD with S/Se powder positioned in the low temperature zone as the source of chalcogens and MoO_3 located at the center of the tube as the Mo source; (b) schematic illustration of the DNA detection based on single-layer Ta_2NiS_5 nanosheets; (c) typical process for the preparation of a $FeNi_2S_4$–graphene–$MoSe_2$ nanocomposite. Reprinted from ref. 23 and 49 with permission from the American Chemical Society and ref. 50 with permission from the Royal Society of Chemistry.

mechanically exfoliated from the bulk by using the CVT method.[58] Tan *et al.* reported the high-yield and scalable preparation of ultrathin 2D TMD nanosheets, including Ta_2NiS_5 and Ta_2NiSe_5, in solution *via* electrochemical Li-intercalation and exfoliation of the layered microflakes. The size of the prepared Ta_2NiS_5 and Ta_2NiS_5 nanosheets ranges from tens of nanometers to a few micrometers (Fig. 2b).[23]

Efforts have been made to find alternative methods of obtaining ternary TMDs. Moreover, PLD, solid-state reactions and hydrothermal methods have been proven to be effective approaches for preparing ternary TMDs. Considering the relatively high growth temperature required for CVD growth that promotes the formation of defects, Yao *et al.* proposed the growth of large-scale and high-quality $Mo_{0.5}W_{0.5}S_2$ alloy films *via* PLD.[61] Moreover, $MoS_{2(1-x)}Se_{2x}$ is obtained using a high-temperature solid-state reaction technique. Typically, $MoS_{2(1-x)}Se_{2x}$ crystals are obtained by heating a mixture of the constituent elements in the required atomic ratio in an evacuated quartz tube at 800 °C for three days.[62] Further, Shen *et al.* designed $FeNi_2S_4$–graphene–MoS_2 and $FeNi_2S_4$–graphene–$MoSe_2$ composites with an *in situ* hydrothermal method (Fig. 2c).[50,63]

2.2 MPTs

The most commonly adopted method of synthesizing MPTs is CVT, which exhibits a high conversion rate of raw materials. Single-crystal $FePS_3$ was grown using this method by Lee *et al.*[64] and Wang *et al.*[65] using pure Fe, P, and S powders. In addition, large single-crystal $MnPS_3$ samples approximately 3.0 × 3.0 mm in size were obtained by using the CVT method with iodine as the transport agent. In this process, stoichiometric amounts of the Mn, P and S powders were used as the reactants, and the reaction was carried out for 120 h in a two-zone electric furnace.[66] Du *et al.* synthesized and exfoliated the bulk crystals of MPS_3 (M = Fe, Mn, Ni, Cd, and Zn) sulphides and $MPSe_3$ (M = Fe and Mn) selenides in MPTs, using the CVT and mechanical exfoliation methods, respectively (Fig. 3a).[59] In fact, the CVT strategy is also applied to prepare other types of MPTs, such as $CoPS_3$ and $SnPS_3$.[67] Note that, in some cases, such as in the synthesis of layered $FePS_3$ and MnPS3, the CVT method is called a solid-state reaction.[68,69] Typically, the conventional CVT process requires a long reaction time, making it inconvenient for practical purposes. In light of this situation, Villanueva *et al.* presented a microwave-assisted preparation of MPS_3 materials (M = Mn and Cd), which shortened the reaction time dramatically, allowing an efficient and rapid synthesis of MPS_3 materials (Fig. 3b).[60]

Additional methods have also been used to obtain MPTs, such as the solvent exfoliation and ion-exchange solvothermal methods. In one case, few-layer $FePS_3$ was obtained using solvent exfoliation developed by Mukherjee *et al.*[70] Furthermore, a polycrystalline nanoparticle sample of $MnPS_3$ was prepared *via* the ion-exchange solvothermal method.[74,75]

2.3 Ternary MXenes

MXenes, a new and potentially very large group, are first synthesized by selectively etching out certain "A" layers from the MAX phases at room temperature (Fig. 4a).[72] The composition of MAX can be expressed as MnAXn-1, where M denotes an early transition metal, A is mainly a group IIIA or IVA element, X is C and/or N, and n = 2–4. As noted, in 2011, Ti_3C_2 was first synthesized by selectively etching the Al atoms in Ti_3AlC_2, using aqueous hydrofluoric acid (HF) at room temperature.[72] The process of Ti_3AlC_2 etching with HF can be summarized as the following simplified reactions:

$$Ti_3AlC_2 + 3HF = AlF_3 + 3/2H_2 + Ti_3C_2 \quad (1)$$

$$Ti_3C_2 + 2H_2O = Ti_3C_2(OH)_2 + H_2 \quad (2)$$

$$Ti_3C_2 + 2HF = Ti_3C_2F_2 + H_2 \quad (3)$$

Reaction (1) is essential and is followed by Reaction (2) and/or (3). Note that by adjusting the etching time and the

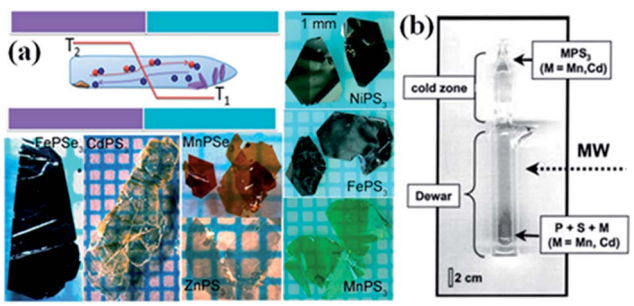

Fig. 3 Methods for preparing MPTs. (a) CVT method and photos of bulk 2D crystals. They are put on the coordinate paper, in which the smallest square is 1 mm × 1 mm; (b) a picture of the Dewar ampoule highlighting its different parts and the process of MPS_3 crystallization. Reprinted from ref. 59 with permission from the American Chemical Society and ref. 60 with permission from Wiley.

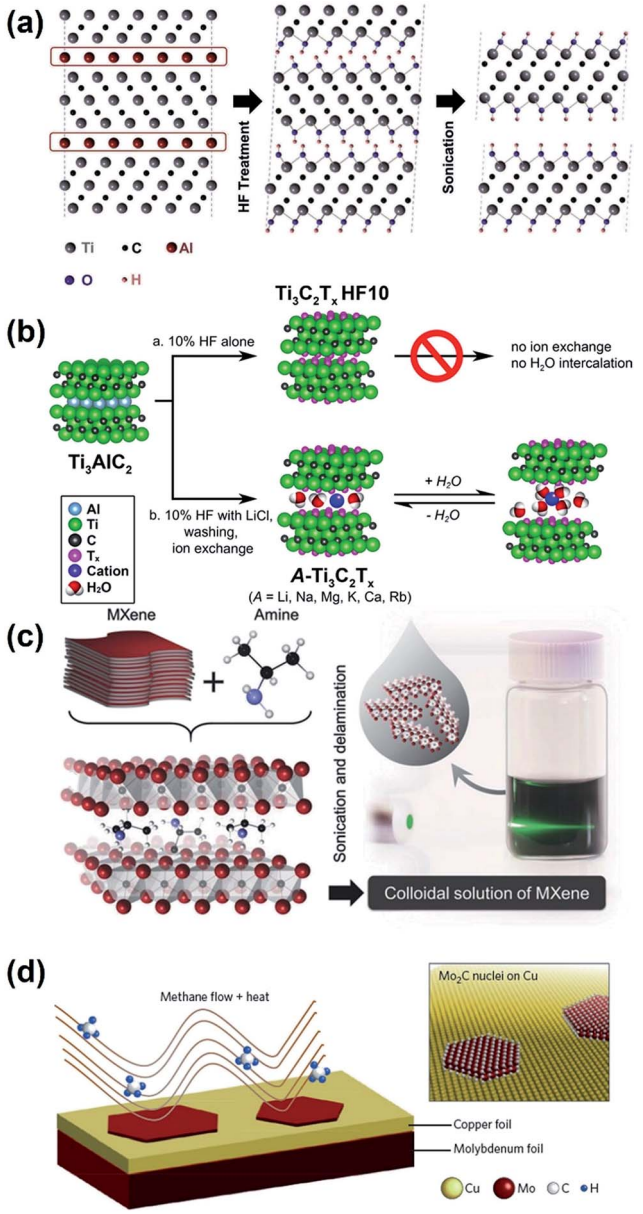

Fig. 4 Methods for preparing MXenes. (a) Schematic of the exfoliation process for Ti_3AlC_2; (b) pathway of materials prepared in this report; (c) schematic of the Nb_2CT_x delamination process *via* isopropylamine intercalation; (d) 2D carbide crystals produced by CVD. Reprinted from ref. 13 with permission from the American Chemical Society; ref. 71 with permission from Nature Publishing Group and ref. 72 and 73 with permission from Wiley.

concentration of HF, numerous MXenes can be synthesized utilizing HF etching from room temperature to 55 °C.[76] Meanwhile, a longer reaction time and stronger etching are required for increasing the atomic numbers of M. This phenomenon may be related to the metallic M–Al bonding,[77] since a larger number of M valence electrons require stronger etching.[78]

The etching process is dependent on kinetics. Therefore, the required etching time is different for various MXenes.[78] Moreover, a complete dissolution or recrystallization of $M_{n+1}X_nT_x$ layers may occur under excessive heating.[79,80]

Except for HF etching, MXenes can also be obtained by using a mixture of a strong acid and a fluoride salt. Ghidiu *et al.* reported a synthesis route to multi-layered $Ti_3C_2T_x$ by immersing Ti_3AlC_2 in a milder etchant solution composed of hydrochloric acid (HCl) and lithium fluoride (LiF) (Fig. 4b).[83–85] The reaction between HCl and LiF can produce HF, which selectively etches the Al atoms. During the etching process *via* metal halide, the MXene layers are intercalated by the cations and water molecules, leading to increased interlayer spacing. Compared with pure HF etching, this method can produce single- or few-layer flakes with high efficiency. For example, Lipatov *et al.* demonstrated an improved method of LiF–HCl selective etching of Ti_3AlC_2, which yields large, high-quality monolayer $Ti_3C_2T_x$ MXene flakes with well-defined and clean edges and visually defect-free surfaces.[86]

To further investigate the 2D properties of the as-prepared multi-layered MXenes, it is imperative and indispensable to obtain single- or few-layer compounds in the production. One effective method to achieve exfoliation is the intercalation of polar organic molecules into the interlayers of MXenes. When DMSO was intercalated into Ti_3C_2 and then sonicated in water, Ti_3C_2 delaminated, forming a stable colloidal solution that was filtered to produce MXene 'paper'.[87] In another case, DMSO was replaced by amine to delaminate the second representative of the MXene family-Nb_2CT_x (Fig. 4c).[73] Naguib *et al.* reported a general approach for the large-scale delamination of MXenes by using a relatively large molecular organic base, namely tetrabutylammonium hydroxide (TBAOH), choline hydroxide, or *n*-butylamine.[88]

Alternative MXene preparation methods have also been explored and chemical vapor deposition (CVD) was proven to be feasible (Fig. 4d).[89] The MXenes prepared by this method have the characteristics of a large lateral dimension and few defects. However, the detailed experimental conditions need to be explored further.

2.4 BCN and other types of ternary 2D materials

BCN is a representative ternary 2D system that was explored prior to the discovery of graphene.[90,91] However, the main obstacle, phase separation, hinders the homogenous synthesis of this material.[47] Although numerous studies have been conducted and methods proposed to obtain h-BCN, obtaining the 'real' BCN without phase separation remains a challenge. The methods of preparing BCN are found to be diverse, among which CVD is the most commonly adopted method. Indeed, by providing the B, C and N sources, the BCN layer can be synthesized.[22,92] A catalyst-free CVD synthesis of BCN nanosheets with a tunable B and N bond structure by thermally decomposing solid urea, boric acid and polyethylene glycol (PEG) precursors was developed.[93] Liu *et al.* demonstrated the epitaxial growth of a single-atomic-layer, in-plane heterostructure of graphene and hexagonal boron nitride (h-BN) by atmospheric-pressure CVD. Interestingly, in this case, the h-BN lattice orientation is only determined by the graphene (Fig. 5a).[81] Gong's group has demonstrated a direct chemical conversion of graphene to high-quality BCN with a full range of

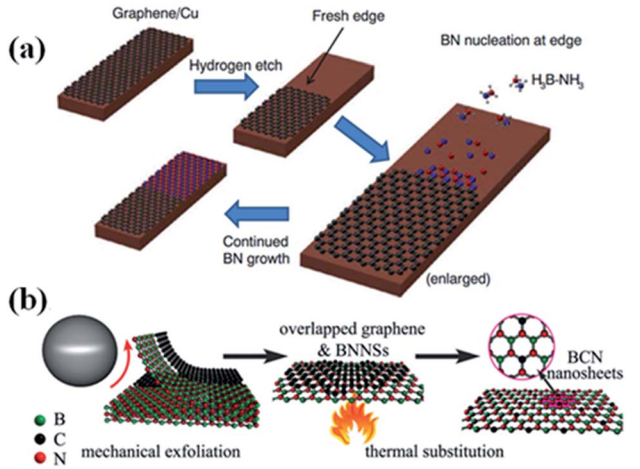

Fig. 5 Methods for preparing BCN. (a) Cartoon illustration of epitaxial growth of BN onto graphene edges; (b) schematic of the processing steps involved in the synthesis of BCN nanosheets. Reprinted from ref. 81 with permission from Science and ref. 82 with permission from the Royal Society of Chemistry.

compositions, which systematically converts conducting graphene into semiconducting ternary h-BCN.[94] This strategy makes it possible to produce uniform BCN structures without disrupting the structural integrity of the original graphene templates.[91,94]

Pulsed laser deposition (PLD), a facile and efficient technique for growing high quality thin films, can control the structure and composition of the as-prepared film. Moreover, compared with CVD, the flammable gas hydrogen is not required for the PLD method. Amorphous BCN films were synthesized by PLD under various laser fluences. The bonding structure of the as-prepared films changed according to the laser fluences.[37] In another study, Zhang *et al.* fabricated BCN films with a large carbon stoichiometric range using PLD with BN-N sources.[95]

Huang *et al.* developed a facile carbon-doping pyrolysis synthesis method to produce BCN nanosheets. In brief, the mixture containing glucose, boron oxide and urea was put into a tube furnace in an ammonia atmosphere for 5 h at 1250 °C.[96] Bulk BCN spheres were deposited on the substrate *via* an organic precursor pyrolysis method. Moreover, BCN materials with a tunable structure, including microspheres and nanoflakes were obtained by controlling the heat treatment of BCN organic precursor pyrolysis.[97,98] Recently, the in-vacuum thermolysis of a single-source precursor, ethane 1,2-diamineborane ($BH_3NH_2CH_2CH_2NH_2BH_3$), was performed to form bulk ternary BCN. The authors aimed to reduce the presence of oxides at the BCN surface, an essential issue linked to many potential applications of BCN materials.[99]

Ma *et al.* proposed a 'thermal substitution' method for preparing BCN nanosheets through substitutional C doping of h-BN nanosheets (Fig. 5b). In comparison to the existing synthesis methods, it has several advantages, such as milder reaction conditions and higher yield. Owing to the adjustable C content of the BCN, a tuned band gap was achieved.[82,98]

Many attempts were made to explore other methods of obtaining BCN, including magnetron sputtering[100] and ion beam-assisted deposition (IBAD).[101] For example, well-adherent BCN thin films with different compositions were grown by the reactive DC magnetron sputtering of a B_4C target with different nitrogen flows.[104] A further example is the deposition of BCN coatings with controlled atomic compositions using the IBAD technique with composite C/B targets.[101]

Beniwal *et al.* utilized thermally induced dehydrogenation of the $B_2N_2C_2H_{12}$ precursor molecules and formed an epitaxial BCN monolayer on Ir (111) through covalent bond formation. In this experiment, atomically flat Ir substrates were exposed under ultrahigh vacuum to bis-BN cyclohexane vapor.[105]

In addition to the materials mentioned above, other types of ternary 2D materials, such as Bi_2O_2Se[106] and $Cr_{1-x}Ge_xTe$, have been reported.[46] Recently, Peng *et al.* reported ultrathin films of non-encapsulated layered Bi_2O_2Se,[106] grown by a home-made low-pressure CVD system, which demonstrate excellent air stability and high-mobility semiconducting behavior. A Hall mobility value of more than 20 000 $cm^2\ V^{-1}\ s^{-1}$ was measured in as-grown Bi_2O_2Se nanoflakes at low temperatures. Bi_2O_3 powder and Bi_2Se_3 bulk were the source materials. The ultrahigh mobility characteristics of Bi_2O_2Se may be more generally applicable to other ternary members (Bi_2O_2S and Bi_2O_2Te) with tunable band gaps. In 2016, Fukuma *et al.* synthesized IV–VI diluted magnetic semiconductor $Ge_{1-x}Cr_xTe$ epilayers on SrF_2 substrates by using the MBE method.[46] The Cr composition increased up to $x = 0.1$, compared with that of $x = 0.06$ on the BaF_2 substrates. The Curie temperature increased with an increase in the Cr composition, and a relatively high value of 200 K was realized in the diluted magnetic semiconductors.

3 Structure, characterization and properties

3.1 Ternary TMDs

Compared with binary TMDs, ternary TMDs enable the control of local electronic structures and provide flexibility to fine tune the specific properties and applications by adding a third element to the structure.[47,58,62,102,103,107–109] Ternary TMDs have a general formula of $M'_aM''_{(1-a)}X_2$ (M′ and M″ are two different transition metals; X = S, Se or Te; $a = 0$ to 1) or $M\ X'_{2a}X''_{2(1-a)}$ (M = transition metals; X′ = S, Se, and Te; X″ = S, Se, and Te; $X' \neq X''$; $a = 0$ to 1).

The structure of MX_2 (M = Mo and W; X = S and Se) is shown in Fig. 6. In MoS_2, each Mo center occupies a trigonal coordination sphere that is bound to six S atoms. Each S atom is connected to three Mo centers. In ternary TMD $Mo_{1-x}W_xS_2$ and $MoS_{2x}Se_{2(1-x)}$, the Mo or S atoms are replaced by the W or Se atoms with different mole ratios.

Xi *et al.*[110] calculated the composition-dependent electronic properties of $Mo_{1-x}W_xS_2$ by using first-principles calculations. The absolute levels of the HOMO and LUMO in $Mo_{1-x}W_xS_2$ were determined by vacuum level calibration (Fig. 7a). As the number of W atoms increases, the HOMO level rises linearly and the LUMO level exhibits an energy bowing, which further lead to the

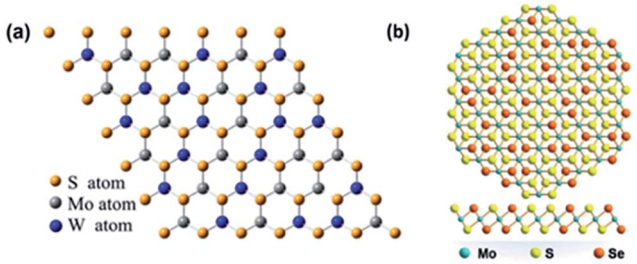

Fig. 6 (a) Structure of $Mo_{1-x}W_xS_2$ ($x = 0.5$). Reprinted from ref. 102 with permission from the American Chemical Society. (b) Structure of $MoS_{2x}Se_{2(1-x)}$. Reprinted from ref. 103 with permission from Wiley.

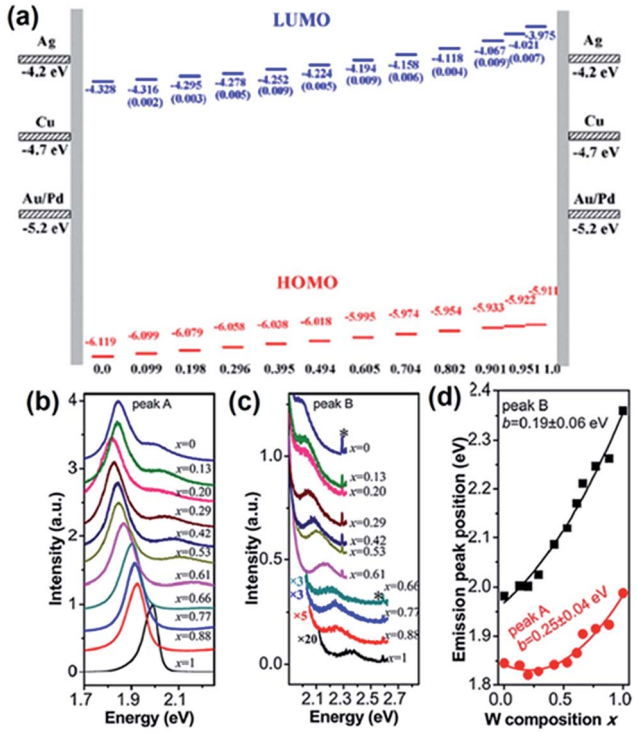

Fig. 7 (a) The absolute energy levels of the HOMO and LUMO for $Mo_{1-x}W_xS_2$ monolayer alloys as a function of W composition x. The number in the bracket is the error bar of the LUMO energy. The Frontier orbital energies are compared to the Fermi levels of four metal electrode materials: Au, Ag, Cu and Pd. Reprinted from ref. 110 with permission from the American Chemical Society. (b–d) Composition-dependent PL emission from $Mo_{1-x}W_xS_2$ monolayers. (b, c) PL spectra of $Mo_{1-x}W_xS_2$ monolayers with different W compositions x. The PL intensity is normalized by the maximum emission intensity. The spectra were excited by 514.5 nm for $x = 0$–0.61 and 457.9 nm for $x =$ 0.66–1. The peaks marked by * are Raman peaks of Si substrates. (d) Composition-dependent emission energies for A and B excitons. The red and black lines are parabola fittings for composition-dependent energy of peaks A and B. Reprinted from ref. 102 with permission from the American Chemical Society.

band gap bowing effect in $Mo_{1-x}W_xS_2$. The experimental band gap changes were observed using PL measurements by Chen *et al.*[102] As the W composition x increases, the A exciton emission red-shifts and then blue-shifts (Fig. 7b). In contrast, the B exciton emission blue-shifts continuously (Fig. 7c). The exciton emission can be tuned from 1.82 to 1.99 eV, whereas the B exciton emission can be tuned from 1.98 to 2.36 eV. The bowing effect can also be seen from the PL measurement. By fitting the experimental data, we can obtain the bowing parameter of 0.25 ± 0.04 eV and 0.19 ± 0.06 eV for A exciton emission and B exciton emission, respectively (Fig. 7d). With increasing selenium content in $MoS_{2x}Se_{2(1-x)}$,[49,62,108] all main diffraction peaks are downshifted continuously (Fig. 8a). Because of the gradual expansion of unit cells upon the substitution of sulphur atoms with larger selenium atoms, the (100) and (110) peaks are downshifted, which implies their mixing at the atomic level. Furthermore, the (103) peak intensity becomes more heightened. From the Raman spectra (Fig. 8b) under 514 nm laser excitation, two sets of composition-dependent vibration modes can be observed: Mo–Se related modes at low frequency (200–300 cm^{-1}) and Mo–S related modes at high frequency (350–410 cm^{-1}), which belong to the typical $MoS_{2x}Se_{2(1-x)}$ alloy.[111,112] With the introduction of selenium, the two vibration modes (E_{2g} at 381 cm^{-1} and A_{1g} at 403 cm^{-1}) shift to a lower frequency. Simultaneously, Mo–Se related modes (E_{2g} at 285 cm^{-1} and A_{1g} at 236 cm^{-1}) start to gain increasing intensity. The PL measurements (Fig. 8c) confirmed the optical band gap change from 1.85 to 1.54 eV with increasing selenium content.

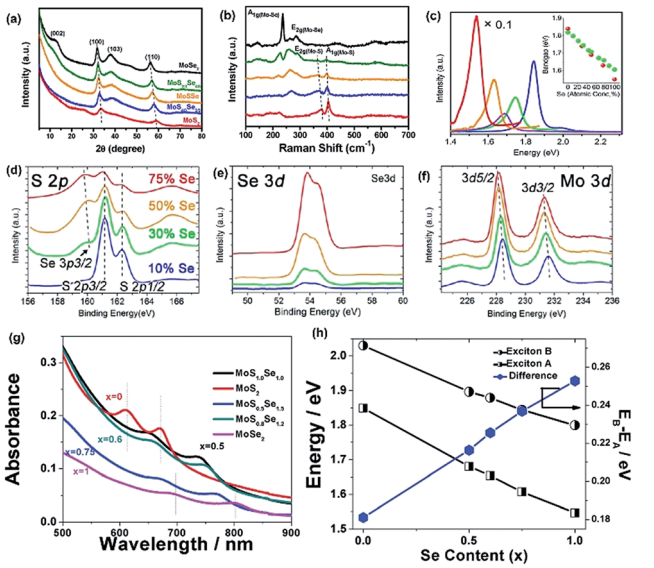

Fig. 8 (a) XRD characterization of $MoS_{2x}Se_{2(1-x)}$. (b) Raman characterization of $MoS_{2x}Se_{2(1-x)}$. (a and b) Reprinted from ref. 108 with permission from the American Chemical Society. (c) PL spectra of pristine MoS_2 (blue), $MoS_{1.4}Se_{0.6}$ (green), MoS_1Se_1 (purple), $MoS_{0.5}Se_{1.5}$ (orange), and $MoSe_2$ (red), measured with a 488 nm laser. Inset: Red dots, the Se concentration dependency of the PL optical gap of $MoS_{2x}Se_{2(1-x)}$ showing a linear decrease from ~1.85 eV (pure MoS_2) to ~1.54 eV (pure $MoSe_2$). (d–f) XPS spectra of S 2p, Se 3d, and Mo 3d core levels in the monolayer $MoS_{2x}Se_{2(1-x)}$ with different Se concentrations ($x = 0.1$, 0.3, 0.50, and 0.75). (c–f) Reprinted from ref. 49 with permission from the American Chemical Society. (g) Absorbance spectra of $MoS_{2x}Se_{2(1-x)}$ with varying x and (h) shows energies of excitons A and B and energy difference of excitons A and B as a function of Se content. (g and h) Reprinted from ref. 62 with permission from the Royal Society of Chemistry.

The optical band gap was linearly dependent on the Se concentration in $MoS_{2x}Se_{2(1-x)}$. This linear dependence was also confirmed by Kiran *et al.* (Fig. 8h).[62] From the XPS results (Fig. 8d–f), with increasing Se concentration, the intensity of the S 2p peaks (~162.3 and 161.2 eV) decreases, whereas peaks from Se $3p_{3/2}$ (~159.8 eV) and Se 3d (~54 eV, Fig. 8e) appear and become dominant.

Yu *et al.*[58] reported that the phase transition from 2H to the 1Td structure occurred in $WSe_{2(1-x)}Te_{2x}$. The crystal structure of 2H $WSe_{2(1-x)}Te_{2x}$ was similar to that of 2H MoS_2, which showed WSe_6 or WSe/Te_6 triangular prism layers bonded together (Fig. 9a). In contrast, in the 1Td $WSe_{2(1-x)}Te_{2x}$ structure, the WTe_6 or WSe/Te_6 octahedra were linked with each other by sharing the Te–Te edges (Fig. 9b). By tuning the concentration of Te from 0% to 100%, 2H $WSe_{2(1-x)}Te_{2x}$ was obtained at $x = 0$–0.4, while 1Td $WSe_{2(1-x)}Te_{2x}$ was obtained at $x = 0.7$–1.0. Interestingly, at $x = 0.5$ to 0.6, an intermediate state appears with two phases (1Td and 2H) (Fig. 9c). The phase transition is confirmed by the PL spectra of the monolayer samples excited with a 532 nm laser. The PL peak continuously shifts from 744 nm to 857 nm (near infrared). No PL signal is detected when $x \geq 0.6$ for the 1Td samples (Fig. 9d). In Fig. 9e, the band gaps are shifted continuously from 1.67 eV to 1.44 eV. Furthermore, the optical gap directly changes from 1.44 to 0 eV when $x \geq 0.6$. This indicates that $WSe_{2(1-x)}Te_{2x}$ alloys undergo a phase transition from semiconductor (2H phase) to metal (1Td phase).

Weyl fermions have been known since the early twentieth century as chiral particles associated with solutions to the Dirac equation at zero mass.[113,114] There is only one type of Weyl fermion in high-energy physics, but exactly two types of Weyl points (WPs)[115] in condensed matter systems. In type-I Weyl semi-metals, the bulk Fermi surface shrinks to a point at the Weyl node, whereas in type-II Weyl semimetals, the Weyl cone arises as a connector of holes and electron pockets, where the large tilt of the cone induces a finite density of states at the node energy. This fundamental difference can, for instance, cause an anomalous Hall effect in type-II Weyl semimetals. Belopolski *et al.*[115,116] reported the experimental discovery of the first type-II Weyl semi-metal in $Mo_xW_{1-x}Te_2$. Then, it was further predicted that a type-II Weyl semi-metal arises in binary and WTe_2.[116,117] Concurrently, $MoTe_2$ and other ternary TMDs were predicted to be Weyl semi-metals.[118] Koepernik *et al.* identified $TaIrTe_4$ as a new member of this family of Weyl semi-metals.[118] $TaIrTe_4$ has the attractive feature that it hosts only four well-separated Weyl points, the minimum imposed by symmetry. Moreover, the topological surface states, Fermi arcs and connecting Weyl nodes of opposite chirality extend to approximately 1/3 of the surface Brillouin zone. This large momentum-space separation is highly favourable for detecting the Fermi arcs spectroscopically and in transport experiments. All three telluride compounds show a minimum set of four Weyl points, occurring at very similar positions in the k space.

3.2 MPTs

Metal phosphorous trichalcogenides (MPTs) have been in existence since the 19th century, and have not been explored comprehensively at the atomically thin level.[120] Their general formula is $M^{II}PX_3$ (M^{II} = Fe, Mn, Zn, Co, Ni, Cd, Mg, *etc.*; X = S and Se) and $M^IM^{III}P_2X_6$ (M^I = Ag and Cu; M^{III} = Cr, V, Al, Ga, In, Bi, *etc.*). The metal of the MPT family is mainly from vanadium to zinc, which has more possible compounds than TMDs (IVB, VB and VIB).[121]

In MPX_3 crystals, each unit cell is composed of two cations and one $[P_2X_6]^{4-}$ cluster. The M atoms are coordinated with six X atoms, while the P atoms are coordinated with three X atoms and one P atom to form a $[P_2S_6]^{4-}$ unit, which is arranged as a honeycomb structure (as shown in Fig. 10a). The atomic layers of the sulphides stack in the $C2/m$ space group (Fig. 10b) while those of the selenide stack in R-3 (Fig. 10c). The two cations can be two M^{II} or one M^I with M^{III}.

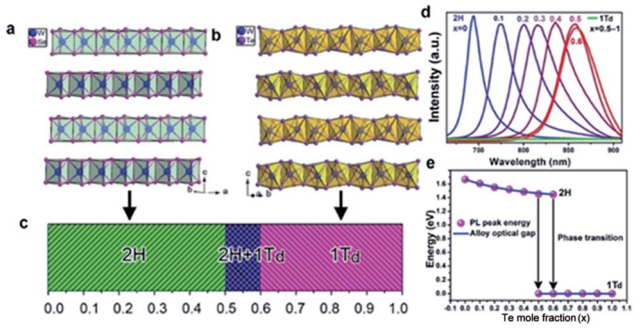

Fig. 9 (a) The crystal structure of 2H WSe_2. (b)The crystal structure of 1Td WTe_2. (c) Different phases with dependence of concentration x in $WSe_{2(1-x)}Te_{2x}$. (d) The PL spectrum of the composition monolayer 2H $WSe_{2(1-x)}Te_{2x}$ ($x = 0$–0.6) alloys. (e) Composition dependent (x) band gaps of the monolayer $WSe_{2(1-x)}Te_{2x}$ ($x = 0$–0.6) alloys. Reprinted from ref. 58 with permission from Wiley.

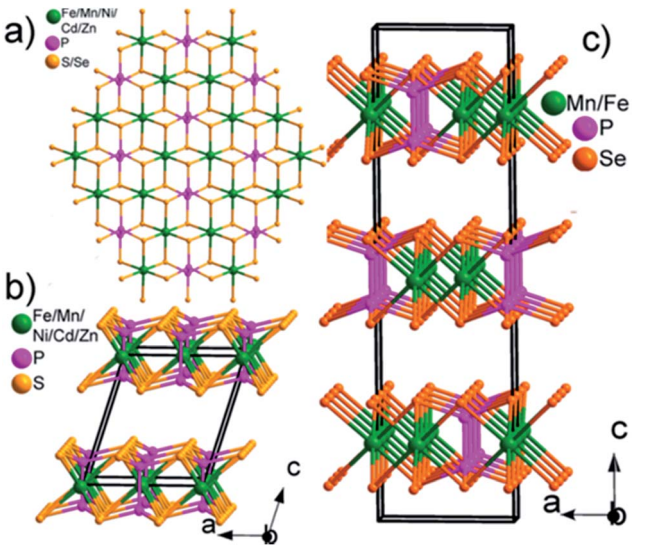

Fig. 10 (a) Arrangement of metal, phosphorus and sulfur or selenium atoms in the plane of MPS_3 (M = Fe, Mn, Ni, Zn and Cd) and $MPSe_3$ (M = Fe and Mn); (b) packing structure of MPS_3; (c) packing structure of $MPSe_3$. Reprinted from ref. 59 with permission from the American Chemical Society.

In bulk MPX_3 crystals, due to the changes of the metal and chalcogenide atoms, the band gap can range from 1.3 to 3.5 eV (Table 1), which indicates a wide wavelength optoelectronic response. From DFT calculations,[122] the monolayer metal phosphorous trichalcogenides have very low formation energies and the band gap can vary in a wide range (Fig. 11a). Meanwhile, the electronic structures are affected greatly by the metal or the chalcogenide atoms. It is interesting that for all the listed monolayer MPX_3 in Fig. 11a, the minimum potentials of the conduction bands are higher than the reduction potential of hydrogen, and the maximum potentials of the valence bands are lower than the oxidation potential of O_2/H_2O. These results indicate that such materials are thermodynamically feasible for both water oxidation and reduction reactions. Furthermore, the strain in monolayer MPX_3 (M = Zn and Cd; X = S and Se) also affects the band structure and further modulates the electronic structures.[123] Transitions between indirect and direct band gaps are observed using compressive strain engineering for $ZnPS_3$, $ZnPSe_3$ and $CdPSe_3$, but not for $CdPS_3$.

The Raman mode of MPS_3 (M = Mn, Fe, Co, Ni, Zn, and Cd) originates from two parts of the structure. One part is attributed

Table 1 Band gap of selected bulk APX_3 (ref. 95 and 119)

Compound	Band gap (eV)
$FePS_3$	1.5
$MnPS_3$	3.0
$NiPS_3$	1.6
$CdPS_3$	3.5
$ZnPS_3$	3.4
$FePSe_3$	1.3
$MnPSe_3$	2.5

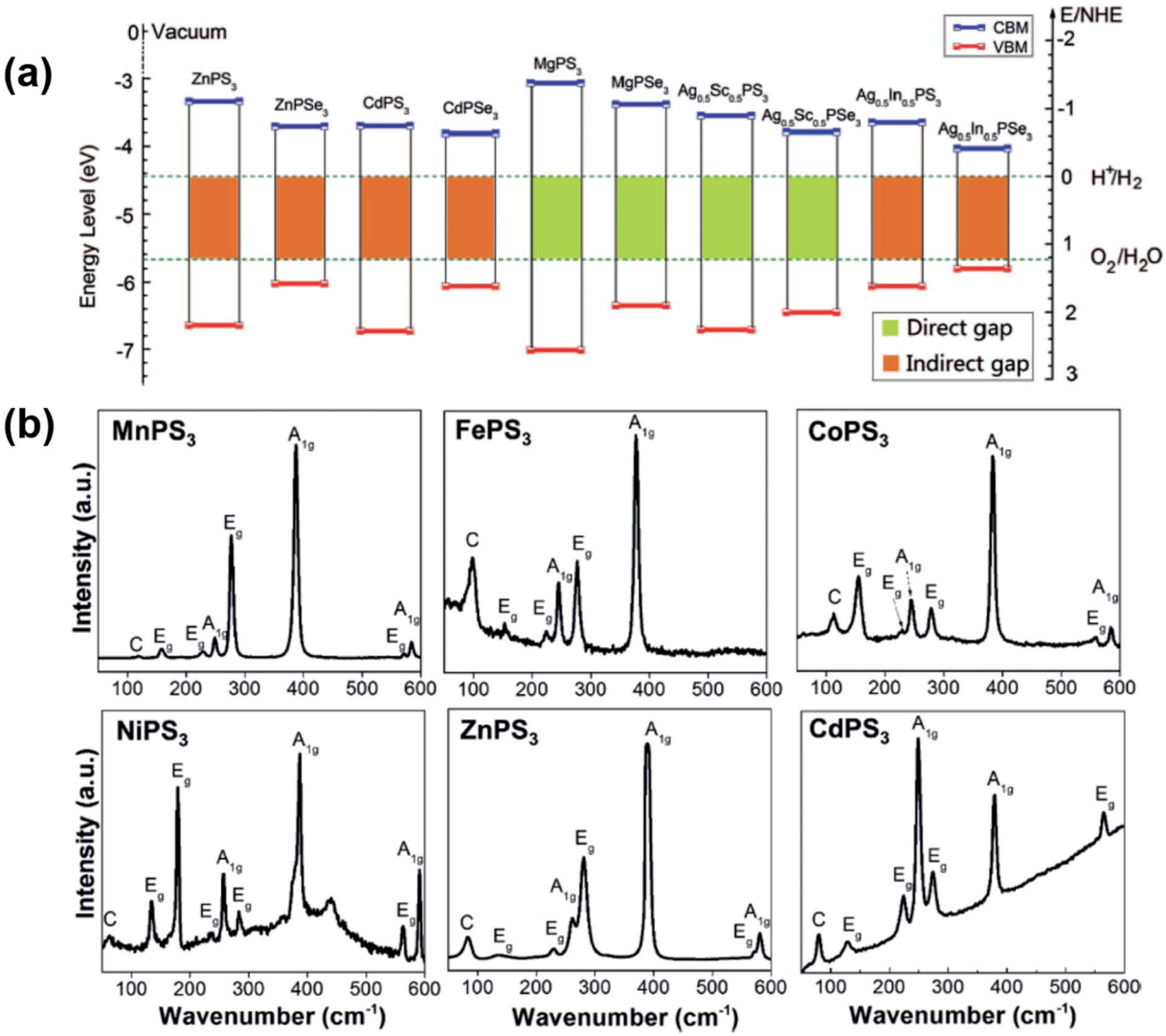

Fig. 11 (a) Band edge positions of single-layer APX_3. The energy scale is indicated by either the normal hydrogen electrode (NHE) (right *Y*-axis) or the vacuum level (left *Y*-axis) in electron volts as a reference. The redox potentials (green dashed line) of water splitting are shown for comparison. Reprinted from ref. 122 with permission from the AIP Publishing. (b) Raman spectrum of transition metal MPS_3 phases. Reprinted from ref. 67 with permission from the American Chemical Society.

to the $[P_2S_6]^{4-}$ cluster and eight Raman active modes with D_{3d} symmetry ($3A_{1g}$ and $5E_g$ Raman active modes).[67] The A_{1g} modes can be observed at around 590, 387 and 255 cm^{-1} and E_g modes at around 560, 283, 235, 180 and 150 cm^{-1}. The overtones of the A_{1g} modes are not observed in all MPS_3 compounds. In particular, they were found in $NiPS_3$ at 815 and 1189 cm^{-1}, at 764 cm^{-1} in $MnPS_3$ and at 1145 cm^{-1} in $ZnPS_3$.[67] The other Raman modes are attributed to the cation vibration.[124,125] The Raman spectra of MPS_3 (M = Mn, Fe, Co, Ni, Zn, and Cd) are shown in Fig. 11b. In $FePS_3$ and $FePSe_3$, the intralayer modes exhibit a slighter Raman shift when the crystal thickness decreases, even to monolayers.[59]

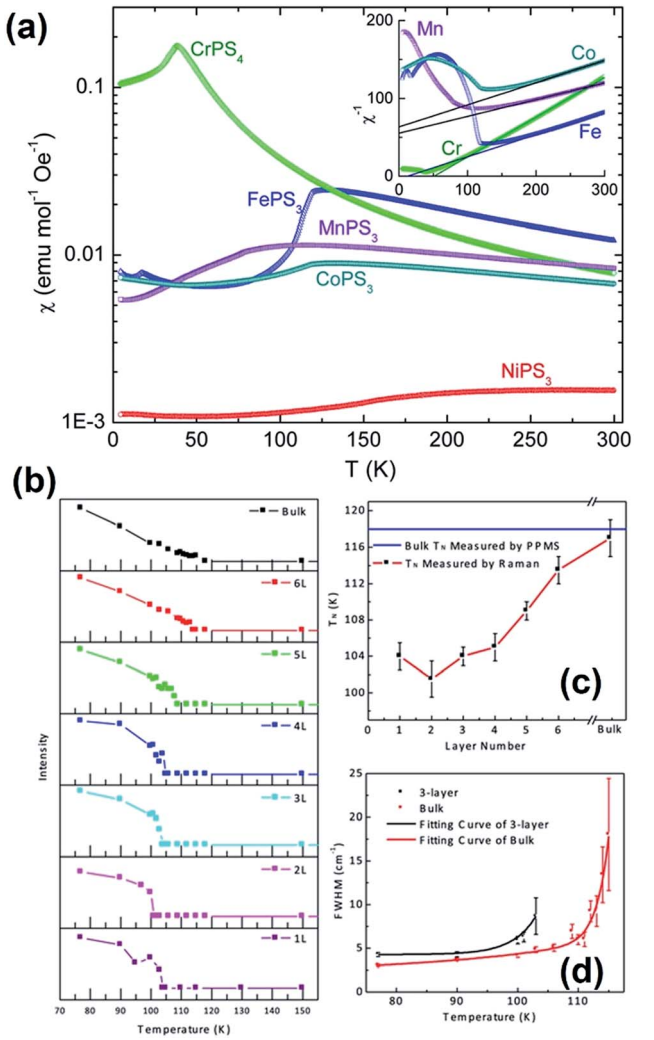

Fig. 12 (a) Magnetic susceptibility of $MnPS_3$, $CoPS_3$, $NiPS_3$, $FePS_3$ and $CrPS_4$ phases measured at a field of 1000 Oe. The inset is the inverse susceptibility representation (without $NiPS_3$). Reprinted from ref. 67 with permission from the American Chemical Society. (b) Plots of intensity of the Raman peak at 88 cm^{-1} *versus* the temperature of samples in different thickness. (c) Plot of Néel temperature (T_N) measured by the optical method *versus* the thickness of samples, compared with the result of the bulk sample measured by PPMS. (d) Plots of the FWHM of the Raman peak at 88 cm^{-1} *versus* the temperature of trilayer and bulk samples. Reprinted from ref. 65 with permission from the IOP Science.

Owing to the difference in the metal atoms in MPX_3, trisulphides with M = Mn, Fe, Co, and Ni undergo a paramagnetic to antiferromagnetic transition with decreasing temperature. However, $SnPS_3$, $ZnPS_3$ and $CdPS_3$ exhibit only diamagnetic behavior. The Néel temperature can be obtained from the magnetic susceptibility measurement (as shown in Fig. 12a). Within the trisulphide series, the Néel temperature increases with an increase in the atomic number and the orbital component enhances the total effective magnetic moment (from the pure spin moment for Mn to the highest orbital moment for Ni).[67] Table 2 summarizes the Néel temperature of MPS_3 (M = Mn, Fe, Co, and Ni) obtained by different measurements. When some MPS_3 crystals are exfoliated down to the monolayer, the Néel temperature decreases. From Table 2, the Néel temperature of bulk $FePS_3$ is approximately 116–120 K. Wang *et al.*[65] reported that the Néel temperature decreased to 104 K for the $FePS_3$ monolayers, as shown in Fig. 12b–d. Furthermore, Toyoshima *et al.*[66] found that the pressure also affects the Néel temperature. The Néel temperature decreased from 86 K to 78 K for $MnPS_3$ bulk crystals at an applied pressure of 0.47 GPa.

3.3 Ternary MXenes

Transition metal carbides, carbonitrides and nitrides (MXenes) are a new class of 2D materials. They have the general formula of $M_nX_{n-1}T_x$ (n = 2–4), where M denotes early transition metals (Sc, Ti, Zr, V, Cr, Mo, *etc.*), X represents carbon and/or nitrogen and T_x indicates surface terminators.[78,127,128] In general, MXenes are obtained by the selective etching of the A element layers from the MAX (M_nAX_{n-1}: M = metal; A = Group IIIA or IVA elements; X = carbon and/or nitrogen) phases at room temperature.[79,129] Due to the etching process, MXenes are always surface terminated with groups such as F, OH, and O after their exfoliation from the MAX phase.[77] Fig. 13 displays the structure of M_nX_{n-1}, which shows n layers of M cover with $n-1$ layers of X in an $[MX]_{n-1}M$ arrangement. When there is more than one metal in the structure, it exhibits two forms: solid solutions and

Table 2 The Néel temperature of MPS_3 (M = Mn, Fe, Co, and Ni)

Compounds	The Néel temperature (T_N) (K)	Method	Reference
$MnPS_3$ (bulk)	82	NMR of ^{31}P	121
	86	Magnetic susceptibility	66
	115	Magnetic susceptibility	67
$FePS_3$ (bulk)	120	Magnetic susceptibility	67
	117	Raman	65
	116	NMR of ^{31}P	121
	117.4	Mössbauer spectroscopy	126
$FePS_3$ (monolayer)	104	Raman	65
$CoPS_3$	122	Neutron diffraction	121
	132	Magnetic susceptibility	67
$NiPS_3$	155	NMR of ^{31}P	121
	265	Magnetic susceptibility	67

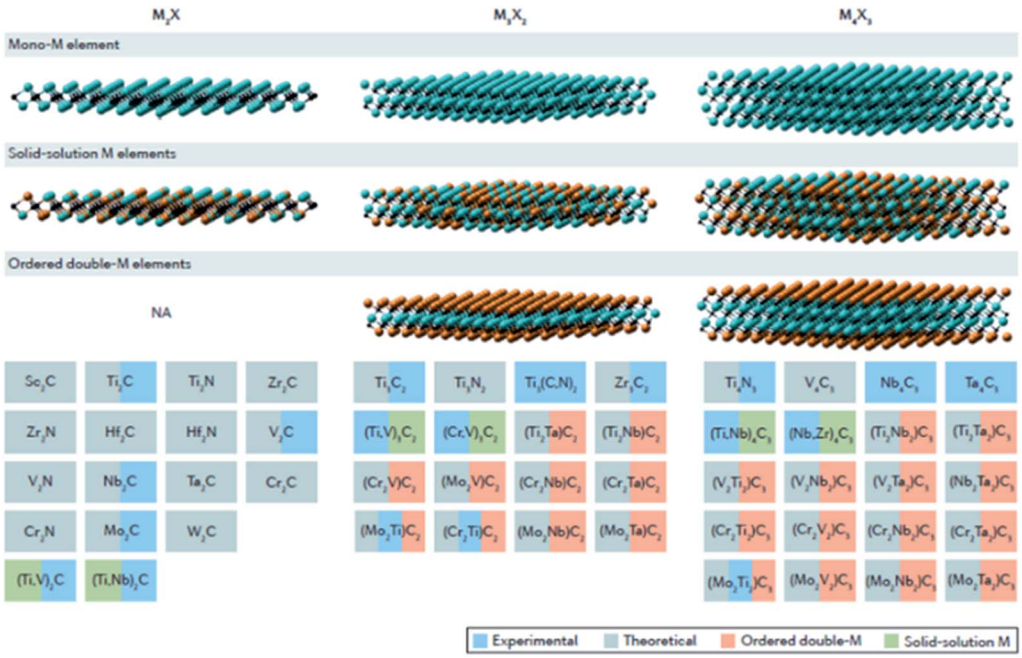

Fig. 13 MXenes reported so far. MXenes can have at least three different formulas: M_2X, M_3X_2 and M_4X_3. They can be made in three different forms: mono-M elements; a solid solution of at least two different M elements; or ordered double-M elements, solid solutions on the X site produce carbonitrides. Reprinted from ref. 78 with permission from Nature Publishing Group.

ordered phases. The two different metals are randomly arranged in solid solution MXenes, while in ordered phases MXenes, single or double layers of one metal are between the layers of a second metal.[78] Through DFT calculations, ordered MXenes have been shown to be energetically more stable than their solid-solution counterparts for certain combinations of transition metals.[130] More than 25 different ordered MXenes have been predicted as shown in Fig. 13. In this review, we only emphasise the properties of ternary (multiple metals) MXenes. Anasori *et al.*[130] reported that more than 25 ternary MXenes have a stable ordered structure, based on DFT calculations. For MXenes with the $M'_2M''C_2$ composition, Mo_2TiC_2, Mo_2VC_2, Mo_2TaC_2, Mo_2NbC_2, Cr_2TiC_2, Cr_2VC_2, Cr_2TaC_2, Cr_2NbC_2, Ti_2NbC_2, Ti_2TaC_2, V_2TaC_2 and V_2TiC_2 have a fully ordered state at 0 K. Moreover, Nb_2VC_2, Ta_2TiC_2, Ta_2VC_2 and Nb_2TiC_2 are more stable in their partially ordered state than in their fully ordered state. In contrast, MXenes with the $M'_2M''_2C_3$ composition, $Mo_2Ti_2C_3$, $Mo_2V_2C_3$, $Mo_2Nb_2C_3$, $Mo_2Ta_2C_3$, $Cr_2Ti_2C_3$, $Cr_2V_2C_3$, $Cr_2Nb_2C_3$, $Cr_2Ta_2C_3$, $Nb_2Ta_2C_3$, $Ti_2Nb_2C_3$, $Ti_2Ta_2C_3$, $V_2Ta_2C_3$, $V_2Nb_2C_3$ and $V_2Ti_2C_3$ are ordered at 0 K. They found that the Mo and Cr atoms avoid the middle layers, whereas Ta and Nb are preferred. Furthermore, in all the cases, the total density of states (DOS) at the Fermi level (E_f) is dominated by the M–M d-orbitals, irrespective of surface termination.

Anasori *et al.*[130] also synthesized Mo_2TiC_2 and $Mo_2Ti_2C_3$ by etching Al from their MAX phases (Mo_2TiAlC_2 and $Mo_2Ti_2AlC_3$, respectively). The synthesis and structure of Mo_2TiC_2 and $Mo_2Ti_2C_3$ are shown in Fig. 14. The MAX phase peaks in the XRD patterns disappeared after etching and the Al signals showed a significant drop, which confirmed the formation of MXenes. The yields of the two compounds are almost 100%. The 3D to 2D transformations in both materials were confirmed using a scanning electron microscope (SEM) and the layers opened after etching. The high-resolution scanning transmission electron microscope (HRSTEM) images of Mo_2TiC_2, $Mo_2Ti_2C_3$, Mo_2TiAlC_2 and $Mo_2Ti_2AlC_3$ clearly show the removal of the Al layers by etching. Mo_2TiC_2 with surface terminators can be delaminated by first intercalating dimethyl sulfoxide (DMSO) and then sonicating in water. After delamination, a stable colloidal solution is obtained, which can be used to form freestanding conductive papers.

Khazaei *et al.*[131] found that $M'_2M''C_2$ compounds (M' = Mo and W; M'' = Ti, Zr, and Hf) with O_2 as the surface terminator are topological insulators. $W_2HfC_2O_2$ shows the largest band gap (0.285 eV). Such large band gaps pave the way for the practical application of topological insulators at room temperature. Furthermore, $M'_2M''_2C_3O_2$ (M' = Mo and W; M'' = Ti and Zr) are topological semi-metals. The first Sc-containing MAX phase was reported by Meshkian *et al.*[132] very recently. Mo_2ScC_2 MXene is obtained by the selective etching of the Al-layers in hydrofluoric acid. It expands the attainable range of MXene compositions and widens the prospects for property tuning.

3.4 BCN and other ternary 2D materials

The h-BCN system is another important type of ternary 2D material. Theoretical calculations[92] indicate that homogenous h-BCN tends to form graphene and h-BN domains separately (Fig. 15a). So far, a homogeneous ternary BCN without phase separation has not been realized. The chemical composition and structure of h-BCN can be analyzed by electron energy-loss spectroscopy (EELS). Three visible edges of h-BCN films were

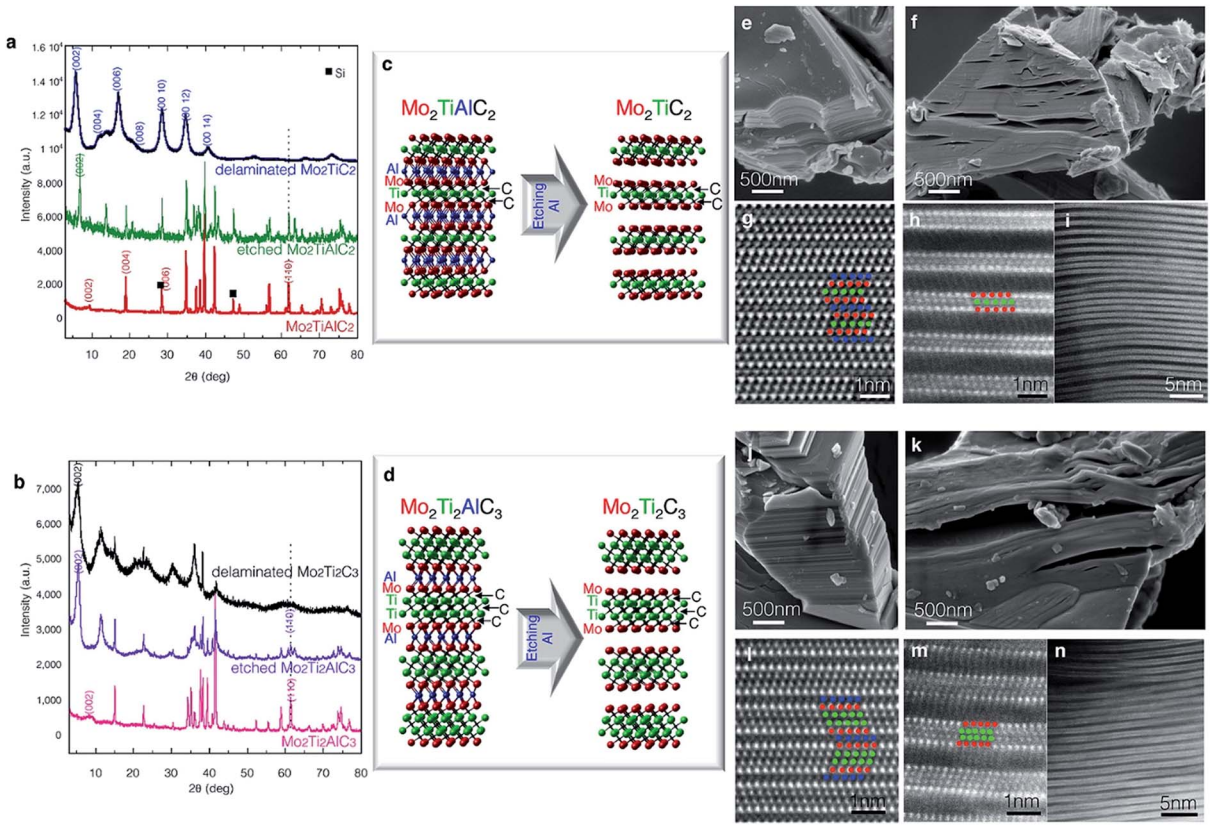

Fig. 14 Synthesis and structure of Mo_2TiC_2 and $Mo_2Ti_2C_3$. (a) XRD patterns of Mo_2TiAlC_2 before and after HF treatment and after delamination. (b) XRD patterns of $Mo_2Ti_2AlC_3$ before and after HF treatment and after delamination. (c and d) Schematics of Mo_2TiAlC_2 to Mo_2TiC_2 and $Mo_2Ti_2AlC_3$ to $Mo_2Ti_2C_3$ transformations, respectively; (e and f) SEM images of Mo_2TiAlC_2 and Mo_2TiC_2, respectively. (g–i) HRSTEM of Mo_2TiAlC_2 and Mo_2TiC_2, respectively. (i) Lower magnification TEM image of (f) showing the layered structure throughout the sample. (j and k) SEM images of $Mo_2Ti_2AlC_3$ and $Mo_2Ti_2C_3$, respectively. HRSTEM images of (l) $Mo_2Ti_2AlC_3$ and (m and n) $Mo_2Ti_2C_3$. Reprinted from ref. 130 with permission from the American Chemical Society.

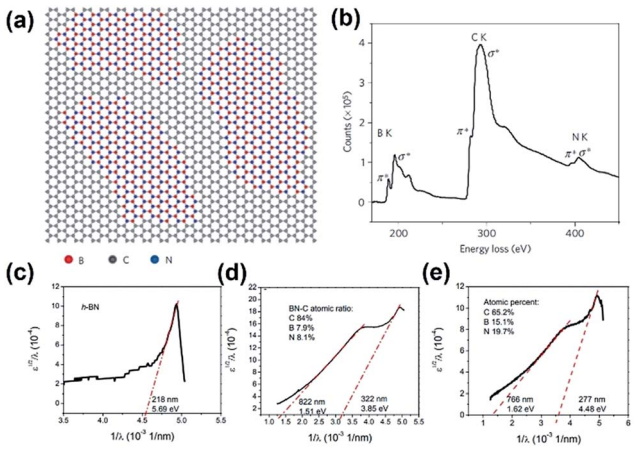

Fig. 15 (a) Atomic model of the h-BNC film showing hybridized h-BN and graphene domains. (b) K-shell excitations of B, C and N are revealed from the core EELS spectra taken from these films. Optical absorption data from the h-BN sample (c), h-BNC sample with 84 at% C (d), and h-BNC sample with 65 at% C (e). Reprinted from ref. 22 with permission from Nature Publishing Group.

observed, starting at 185, 276 and 393 eV (Fig. 15b), which corresponded to the characteristic K-shell ionization edges of B, C and N, respectively.[22,133] Furthermore, such types of EELS edge structures indicate that all three elements are sp^2 hybridized.[133] Owing to domain separation, the band gap engineering can be tuned by controlling the concentration of carbon. The optical band gap of h-BCN with different domain concentrations was measured by ultraviolet-visible absorption spectra (Fig. 15c–e). The h-BN sample shows one absorption edge at 218 nm, which corresponds to an optical band gap of 5.69 eV (Fig. 15c). With C concentrations of 65 at% and 84 at%, the band gaps are 4.48 and 3.85 eV, respectively. This indicates that the band gap decreases with a decrease in the h-BN domain. Furthermore, a second absorption edge was observed, which corresponds to the optical band gap of 1.62 and 1.51 eV from the samples with 65 and 84 at% C, respectively. This absorption edge can be assigned to the h-BN-doped graphene domains.

Wu *et al.*[134] reported a new ternary 2D material (Bi_2O_2Se) with an ultrahigh Hall mobility of >20 000 $cm^2\ V^{-1}\ s^{-1}$ at low temperatures. It shows a tetragonal structure with the *I*4/*mmm* space group and consists of Bi_2O_2 planar covalent layers sandwiched by Se atoms with relatively weak electrostatic interactions (Fig. 16a). It does not show standard van der Waals gaps compared with TMDs. Therefore, the cleavage should be along the Se planes, which results in a possible rearrangement of the surface atomic structure. Bi_2O_2Se preferentially crystallizes onto a mica substrate with a large lateral size. Fig. 16b shows the

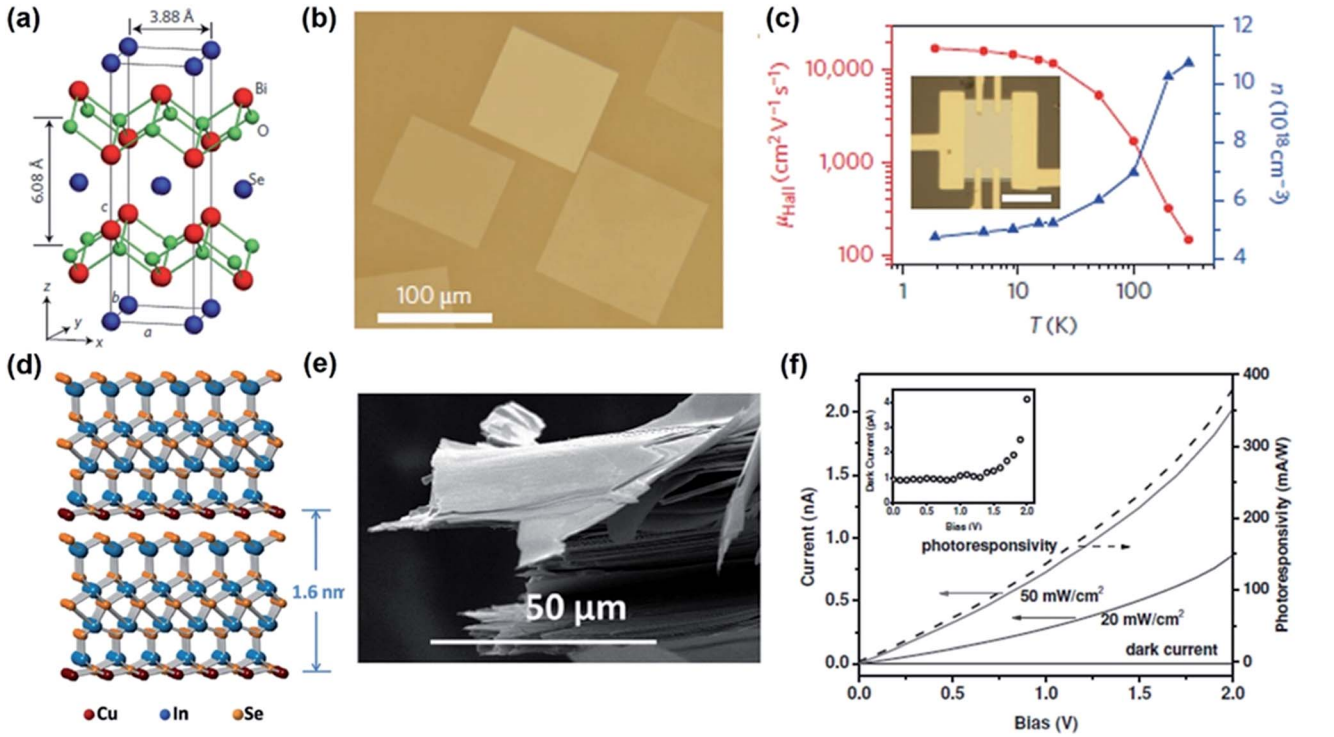

Fig. 16 (a) Layered crystal structure of Bi_2O_2Se with tetragonal $(Bi_2O_2)_n$ layers and Se_n layers alternately stacked along the *c* axis. (b) Typical optical microscopy image of square Bi_2O_2Se nanoplates grown on mica. (c) Hall mobility and carrier density as a function of temperature in a Bi_2O_2Se nanoplate. Inset: optical microscopy image of a Hall-bar device fabricated on the Bi_2O_2Se nanoplate with a thickness of ~20.9 nm. (a–c) Reprinted from ref. 134 with permission from Nature Publishing Group. (d) Crystal structure model of $CuIn_7Se_{11}$. A single-layered $CuIn_7Se_{11}$ contains 5 layers of metallic ions. (e) Scanning electron microscope (SEM) image of a $CuIn_7Se_{11}$ crystal. (f) Photoconductivity IV curves of the $CuIn_7Se_{11}$ photodetector. (d–f) Reprinted from ref. 25 with permission from Wiley.

morphology of Bi_2O_2Se, which exhibits a square shape and ultra-flat surfaces. The temperature dependence of Hall mobility is shown in Fig. 16c. Bi_2O_2Se flakes exhibit the electron Hall mobility of 18 500–28 900 $cm^2\ V^{-1}\ s^{-1}$ at 1.9 K. Lei *et al.*[25] reported another ternary copper indium selenide 2D material ($CuIn_7Se_{11}$) with a good photo-response. The side view of the $CuIn_7Se_{11}$ structure is shown in Fig. 16d. The inter-layer distance in this material is 1.6 nm and it shows standard van der Waals gaps between layers. This layer structure is confirmed by SEM, as shown in Fig. 16e, which indicates a weak interlayer interaction. Fig. 16f shows the photo-response of the few-layer $CuIn_7Se_{11}$. The dark current of the device is in the order of 1 pA, which is very low compared to most layered material based photodetectors.[27,33] When $CuIn_7Se_{11}$ is illuminated by a 543 nm laser with intensities of 20 mW cm^{-2} and 50 mW cm^{-2}, the device shows a strong photo-response.

Very recently, Gong *et al.*[135] reported a long-range ferromagnetic order in pristine $Cr_2Ge_2Te_6$ van der Waals crystals. By the investigation of the temperature and magnetic-field-dependent Kerr effect *via* scanning magneto-optic Kerr microscopy, the ferromagnetic transition temperature was controlled. The crystal structure (side and top views) of $Cr_2Ge_2Te_6$ is shown in Fig. 17a. $Cr_2Ge_2Te_6$ is a new layered material belonging to the lamellar ternary $M_2X_2Te_6$ chalcogenide family (where M denotes a +3 oxidation state metal and X_2 represents a silicon or a germanium pair). It has an interlayer van der Waals spacing of 3.4 Å. Schematic representations of the magnon density of states per spin around the low-energy band edge of the monolayer, multi-layer and bulk ferromagnetic materials are presented in Fig. 17b–d. These figures show that the density of states per spin for the magnon modes near the excitation gap is rapidly reduced. Fig. 17e shows the transition temperatures T_C of samples of different thicknesses, obtained from the Kerr measurements (blue squares) and theoretical calculations (red circles). A strong dimensionality effect is observed, in line with the experimental observations. A ferromagnetic hysteresis loop with single-domain remanence in a six-layer $Cr_2Ge_2Te_6$ crystal is shown in Fig. 17f. The almost saturated Kerr signal at 0.6 T shows approximately 75 μrad per layer. Under a magnetic field, there is a clear contrast between the insensitivity of the transition temperature of the three-dimensional system. By using the renormalized spin wave theory to analyze the observed phenomena, we concluded that the relationship between the transition temperature and the magnetic field is the intrinsic specificity of the 2D ferromagnetic molecular crystal. In this 2D molecular ferromagnetic material, for the first time, a very small magnetic field (less than 0.3 T) was used to achieve transition temperature (ferromagnetic and paramagnetic state transition between the temperatures) regulation. Their experimental observations may provide a generic understanding of the ferromagnetic behavior of many soft, 2D van der Waals ferromagnets, such as $Cr_2Si_2Te_6$ and CrI_3.

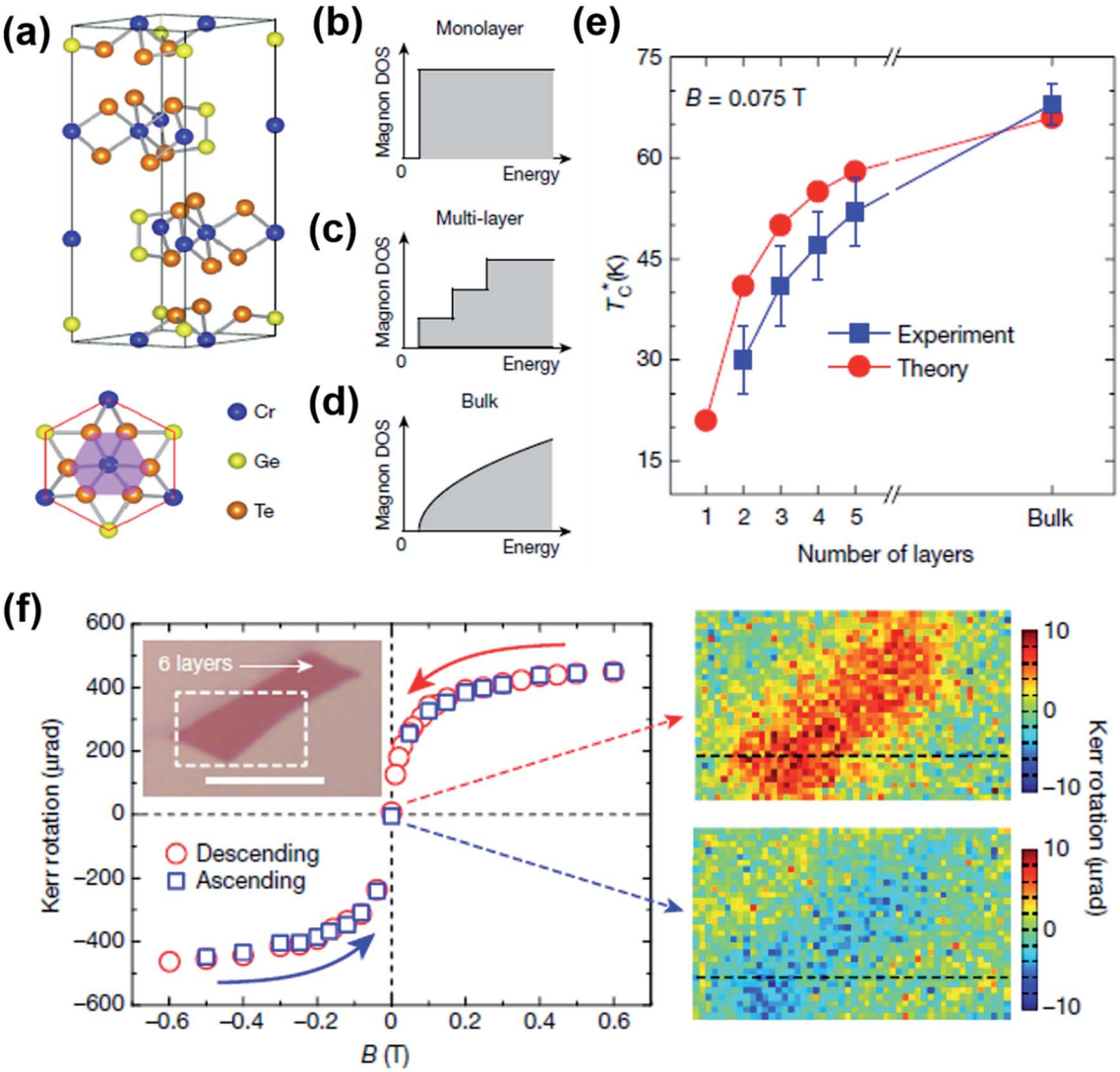

Fig. 17 (a) Crystal structure (side and top views) of $Cr_2Ge_2Te_6$. (b–d) Schematics of magnon density of states (DOS) per spin around the low-energy band edge of monolayer (c), multi-layer (d) and bulk (e) ferromagnetic materials. (e) Transition temperatures T_C^* (defined in text) of samples of different thicknesses, obtained from Kerr measurements (blue squares) and theoretical calculations (red circles). (f) Hysteresis loop of a six-layer flake at 4.7 K showing a saturating trend at 0.6 T and small non-vanishing remanence. The solid red (blue) arrow represents the descending (ascending) field. The loop starts from 0.6 T. Inset, optical image of the flake; scale bar, 10 μm. Reprinted from ref. 135 with permission from Nature Publishing Group.

4 Potential applications

4.1 Energy storage

Energy storage is an important application of 2D materials. Batteries and supercapacitors are two main types of energy storage devices. Extensive studies have been reported for binary 2D materials; however, as far as we know, only a few reports have been published for ternary 2D materials. Since their discovery, MXenes have been explored for use as anodes in lithium-ion batteries (LIBs) and sodium-ion batteries (SIBs) as well as for supercapacitor and pseudo-capacitor applications owing to their promising features such as sufficiently large electrochemically active surfaces, excellent electrical conductivity, exceptional mechanical properties and tunable band gap energies. In addition, the structure of layered MXenes not only allows the intercalation of a variety of organic and inorganic molecules/ions but also disperses easily in aqueous solutions (hydrophilic).[128,136–139] DFT calculations predict that a higher formula unit of MXenes leads to a fast diffusion rate but low reversible capacity as compared to that of the lower formula unit, and *vice versa*.[140] Ternary MXenes, in accordance with their binary analogues, exhibit a striking ability to store Li^+/Na^+ and exhibit a superior specific capacity with improved stability.

To date, limited ternary MXene materials, such as Mo_2ScC_2, $(Nb_{0.8}Ti_{0.2})_4C_3T_x$ and $(Nb_{0.8}Zr_{0.2})_4C_3T_x$,[132,138,141] have been studied for energy storage applications. Barsoum *et al.*[142] reported two Nb_4AlC_3-based solid solution MAX phases $(Nb_{0.8}Ti_{0.2})_4AlC_3$ and $(Nb_{0.8}Zr_{0.2})_4AlC_3$, and their corresponding

MXenes, $(Nb_{0.8}Ti_{0.2})_4C_3T_x$ and $(Nb_{0.8}Zr_{0.2})_4C_3T_x$, were synthesized. Substituting 20 at% of Nb atoms with Ti or Zr atoms did not result in significant changes in the Li uptake compared with $Nb_4C_3T_x$. $(Nb_{0.8}Ti_{0.2})_4C_3T_x$ and $(Nb_{0.8}Zr_{0.2})_4C_3T_x$ retained the specific capacities of 158 and 132 mA h g^{-1} after 20 cycles, respectively.

Barsoum *et al.*[130] synthesized Mo_2TiC_2, $Mo_2Ti_2C_3$ and Cr_2TiC_2 ternary MXenes, and explored the potential of Mo_2TiC_2 with respect to electrochemical energy storage. The $Mo_2TiC_2T_x$ electrode showed a stable capacity of about 176 mA h g^{-1} in the second cycle and retained about 82% of this capacity after 160 cycles (Fig. 18). About 92% of the 260 mA h g^{-1} capacity was retained after 25 cycles at C/10. At both rates, coulombic efficiencies higher than 97% were observed after the first cycle. Considering that more than 20 theoretically predicted members belong to the ternary system, further exploration regarding electrochemical performance with various MXenes is expected.

As early as 1977, Thompson *et al.*[143] used $NiPS_3$ as a cathode in Li-ion batteries. $NiPS_3$ has a capacitance of 1 kWh kg and a capacity retention of 30% after 300 cycles. Following this, Kuz'minskii *et al.*[144] investigated the electrochemical properties of the layered $NiPS_3$ compound at 200 °C. They found that the reversible behavior of the $NiPS_3$ electrode was possible during the charge/discharge cycles within the $0 \leq Li/Ni \leq 3$ range.

Even though numerous reports on binary TMDs for applications in batteries and supercapacitors have been published,[50,145–147] limited research was found on ternary TMDs. Zhang *et al.*[148] developed a novel and effective strategy to distort the lattice structure of MoSSe and tune its properties for Li–O_2 batteries (Fig. 19). The Li–O_2 batteries can deliver a high discharge capacity of 708.24 mA h g^{-1} for a metastable MoSSe solid solution at the current density of 50 mA g^{-1}. Further, they also showed a high specific capacity of ~730 mA h g^{-1} with stable discharge–charge overpotentials (0.17/0.49 V) over 30 cycles.

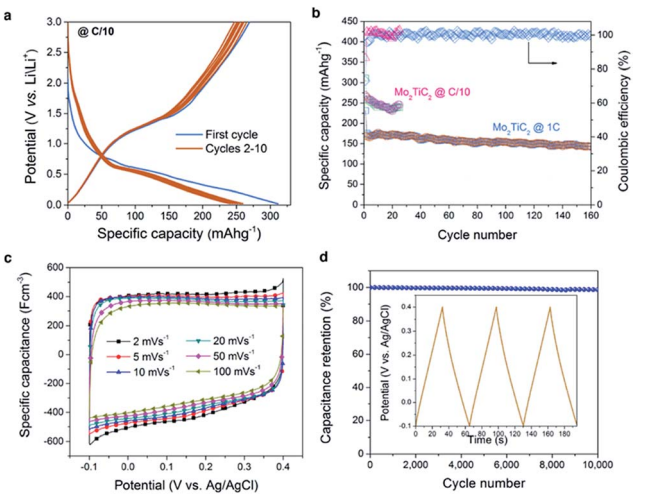

Fig. 18 Electrochemical performance of Mo_2TiC_2 in LIB and supercapacitor electrodes. (a) Voltage profiles between 0.02 and 3 V *vs.* Li/Li^+ at C/10 rate for the first 10 cycles. (b) Specific lithiation (squares) and delithiation (circles) capacities *versus* cycle number at 1C and C/10 rates. Right axis in panel (b) shows the coulombic efficiencies of cells tested at these rates. (c) Cyclic voltammograms, at different scan rates, for a freestanding electrode in 1 M H_2SO_4. (d) Capacitance retention test of Mo_2TiC_2 'paper' in 1 M H_2SO_4. Inset shows galvanostatic cycling data collected at a current density of 1 A g^{-1}. Reprinted from ref. 130 with permission from the American Chemical Society.

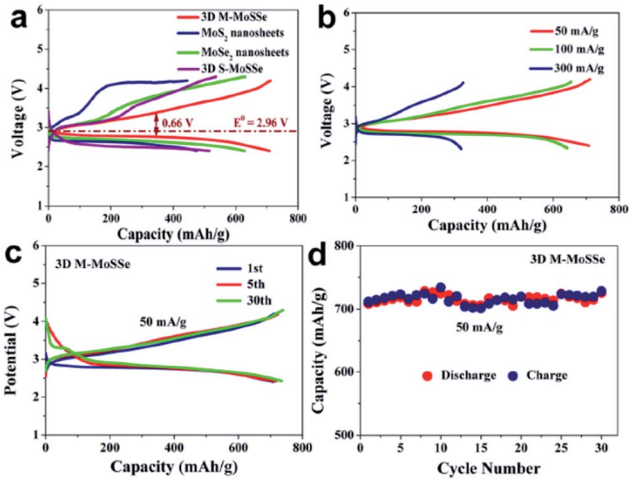

Fig. 19 (a) The first cycle discharge–charge profile of the MoS_2, $MoSe_2$, 3D S–MoSSe, and 3D M–MoSSe cathode at a current density of 50 mA g^{-1}. (b) Galvanostatic discharge and charge curves of the 3D metastable MoSSe cathode in the first cycle at current densities from 50 to 300 mA g^{-1}. (c) Full discharge–charge profiles of the Li–O_2 batteries with the 3D M–MoSSe cathode. (d) The cycling stability of the Li–O_2 cell with the 3D metastable MoSSe cathode. Reprinted from ref. 148 with permission from the American Chemical Society.

4.2 Electrocatalysts

Hydrogen is the most environmentally friendly fuel with the largest energy density, and may be the world's primary fuel source in the future.[149] However, hydrogen is not found naturally in the high-density gas form.[127] Water splitting is an important clean energy technology to produce hydrogen. It involves the oxygen evolution reaction (OER) ($2H_2O \rightarrow 4e^- + 4H^+ + O_2$) and hydrogen evolution reaction (HER) ($2H^+ + 2e^- \rightarrow H_2$). Platinum is the most efficient catalyst for the HER (Tafel slope: 29 mV per dec).[54] However, platinum is quite expensive and the resource is limited, and therefore, the usage is restricted.[150–152] Despite the fact that many binary MXene studies have been reported on the HER application,[153–155] the reports on ternary MXenes are rather rare. In this section, we emphasize MPTs and TTMDs.

From DFT calculations,[122] metal phosphorous trichalcogenides were found to have the potential to be used in the HER and OER. Pumera *et al.*[67] reported the HER, OER and oxygen reduction reaction (ORR) for several metal phosphorous trichalcogenides (Fig. 20). The onset potentials of $NiPS_3$ (−0.53 V *vs.* the RHE), $CoPS_3$ (−0.59 V *vs.* the RHE), and $FePS_3$ (−0.86 V *vs.* the RHE) lie between the onset potentials of Pt (−0.103 V *vs.* the RHE) and glassy carbon (GC) (−0.89 V *vs.* the RHE). The high HER activity for $NiPS_3$ and $CoPS_3$ may be attributed to the crystal structure. The highest catalytic efficiency was observed for $NiPS_3$ with a Tafel slope at an average of

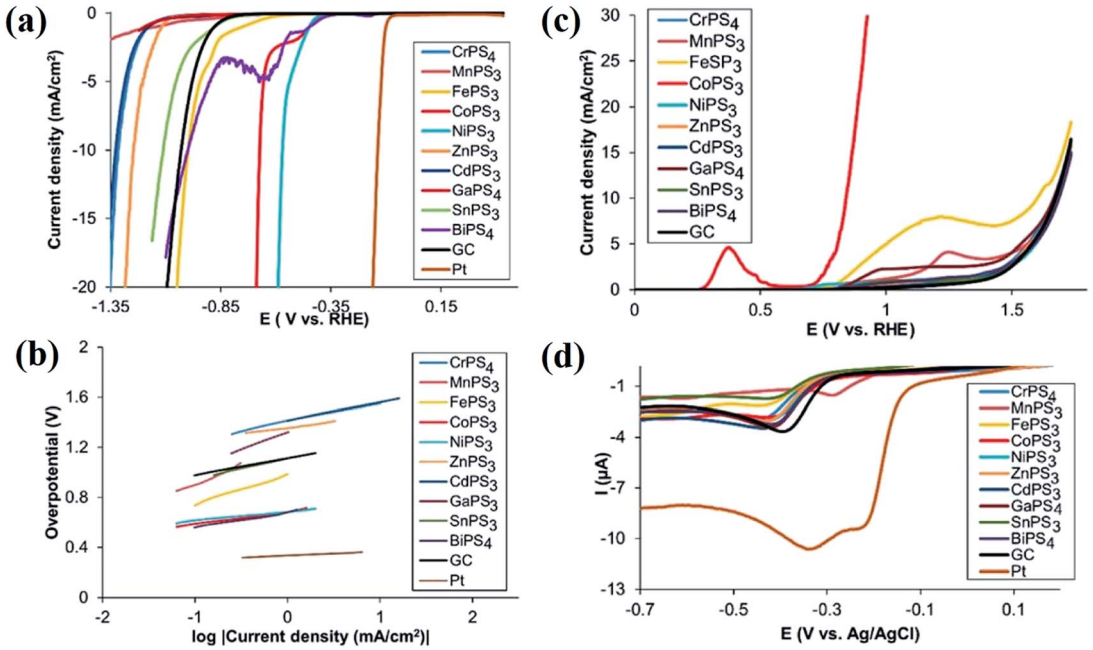

Fig. 20 Linear sweep voltammograms (a) and Tafel plots (b) of the hydrogen evolution reaction (HER) of several MPTs. LSV of the oxygen evolution reaction (OER) (c) and LSV of the oxygen reduction reaction (ORR) (d) of several MPTs. Reprinted from ref. 67 with permission from the American Chemical Society.

~56 mV per dec. In addition, $ZnPS_3$ (75 mV per dec) and $CoPS_3$ (84 mV per dec) have a Tafel slope less than 100 mV per dec. The best catalytic performance for the OER was observed on $CoPS_3$ with an onset potential of 0.84 V at 10 mA cm^{-2}, and the current density reached 30 mA cm^{-2}. However, other materials exhibited lower OER activities. The best performance of the ORR is observed in $MnPS_3$. The reduction peak was at about −0.28 V *vs.* the RHE, while for Pt the reduction peak was at about −0.21 V *vs.* the RHE.

Various binary TMDs, particularly MoS_2 and WS_2, have been confirmed to be efficient non-Pt catalysts for the HER.[158–163] It is easy to tune the electronic structure of $MS_{2x}Se_{2(1-x)}$ (M = Mo, W, and Co) upon Se/S incorporation, which probably further assists in the realization of high HER activity.[54,62,108] Kiran *et al.*[62] reported the HER properties of MoSSe. MoSSe has a more positive onset potential for the HER than the few-layer pristine MoS_2 and $MoSe_2$ nanosheets. A typical Tafel slope obtained for MoSSe is 56 mV per dec, which is quite smaller than that of MoS_2 (96 mV per dec) and $MoSe_2$ (95 mV per dec). Konkena *et al.*[54] synthesized MoSSe@reduced graphene oxide (r-GO) nanocomposite heterostructures to further improve the HER performance. The onset potential of the MoSSe@r-GO composite nanostructures further positively shifted. The enhanced catalytic activity was realized owing to the superior electron transfer efficiency caused by the electronic conductivity of r-GO. The Tafel slopes of the MoSSe@rGO composite and MoSSe are 51 and 63 mV per dec, respectively. Such low Tafel slopes indicate faster reaction kinetics during hydrogen evolution than in the case of MoSS nanosheets.

Xu *et al.*[156] synthesized $WS_{2x}Se_{2(1-x)}$ nanotubes and investigated the HER performance. $MoS_{2x}Se_{2(1-x)}$ ($x = 0.48$) shows the best HER catalytic activity among all electrocatalysts shown in Fig. 21a. Both the increased number of active sites and higher conductivity of $MoS_{2x}Se_{2(1-x)}$ ($x = 0.48$) are responsible for the good HER performance. The Tafel slopes (Fig. 21b) of the WSe_2 and $MoS_{2x}Se_{2(1-x)}$ ($x = 0.48$) are 99 and 105 mV per dec, respectively, which are lower than that of WS_2 (113 mV per dec).[164]

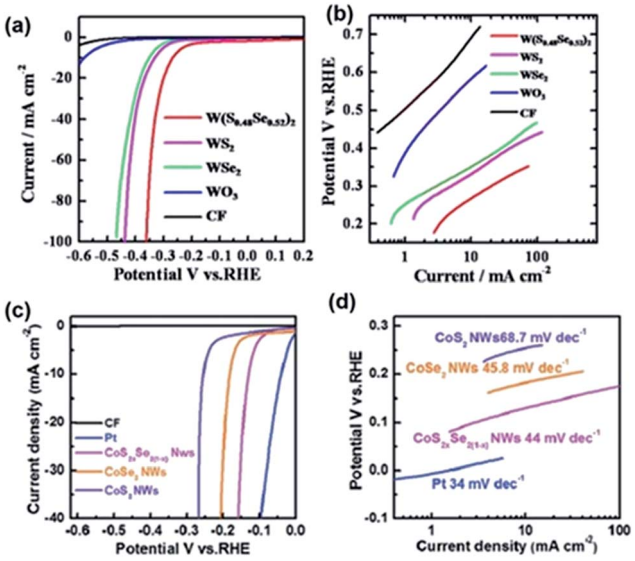

Fig. 21 Linear sweep voltammograms (a) and Tafel plots (b) of the hydrogen evolution reaction (HER) for $WS_{2x}Se_{2(1-x)}$. (a and b) Reprinted from ref. 156 with permission from the American Chemical Society. Linear sweep voltammograms (c) and Tafel plots (d) of the hydrogen evolution reaction (HER) for $CoS_{2x}Se_{2(1-x)}$. (c and d) Reprinted from ref. 157 with permission from the Royal Society of Chemistry.

Liu *et al.*[157] presented the HER performance of $CoS_{2x}Se_{2(1-x)}$ nanowires (Fig. 21c and d). $MoS_{2x}Se_{2(1-x)}$ ($x = 0.67$) shows a more positive onset potential for the HER than the CoS_2 and $CoSe_2$ nanowires. The linear parts of the Tafel plots reveal a low Tafel slope of 44 mV per dec for $MoS_{2x}Se_{2(1-x)}$ ($x = 0.67$), which is lower than that of CoS_2 (68.7 mV per dec) and $CoSe_2$ (45.8 mV per dec). This may be due to the optimal electronic structure of the catalyst incorporating S and Se atoms.[165]

4.3 Other applications

Owing to their unique structure and properties, ternary 2D systems are good candidates for investigating device applications, such as photodetectors, solar cells, sensors and FETs. Thus, it is important to fabricate high-performance devices using ternary 2D materials. Ternary copper indium selenide has a high photoresponsivity and wide spectral response range, and it has been intensively investigated for application in photodetectors. Ajayan *et al.* successfully synthesized and isolated high-quality few-layered flakes of ternary $CuIn_7Se_{11}$, and characterized their photocurrent properties using photoconductivity measurements (Fig. 22).[25] Atomically layered $CuIn_7Se_{11}$ (CIS) with Ti/Au electrodes shows an excellent photoresponse with a low dark current of 1 pA, an S/N larger than 95 dB for 1 mW cm^{-2} 543 nm illumination, a relatively fast response time of 24 ms and a large linear dynamic range of 70 dB. These properties indicate that atomically layered $CuIn_7Se_{11}$ is a very good candidate for 2D photodetectors. Further, they demonstrated 2D $CuIn_7Se_{11}$ photovoltaic devices based on an asymmetric Schottky junction architecture. They observed a 2D photovoltaic effect with a power efficiency of 0.04% and an IPCE of 1.7%. This device performance can be readily improved by optimizing the electrode materials and channel lengths. Their study shows that layered $CuIn_7Se_{11}$ is a highly promising ternary platform for atomically layered optoelectronic device development.

The electronic and photo-responsive properties of atomically thin ReSSe were reported by Liu *et al.*[109] They made an n-type few-layered ReSSe transistor, and the electron mobility was found to be about 3 $cm^2 V^{-1} s^{-1}$. Because of the direct band gap nature of ReSSe, photosensitive devices based on few-layer ReSSe exhibit a very high photo-responsivity, up to 8 AW^{-1}. In combination with large-area material preparation methods such as liquid scale exfoliation or chemical vapour deposition, the composition-dependent band gaps of ReSSe alloys make ReSSe a promising material for optoelectronic applications and

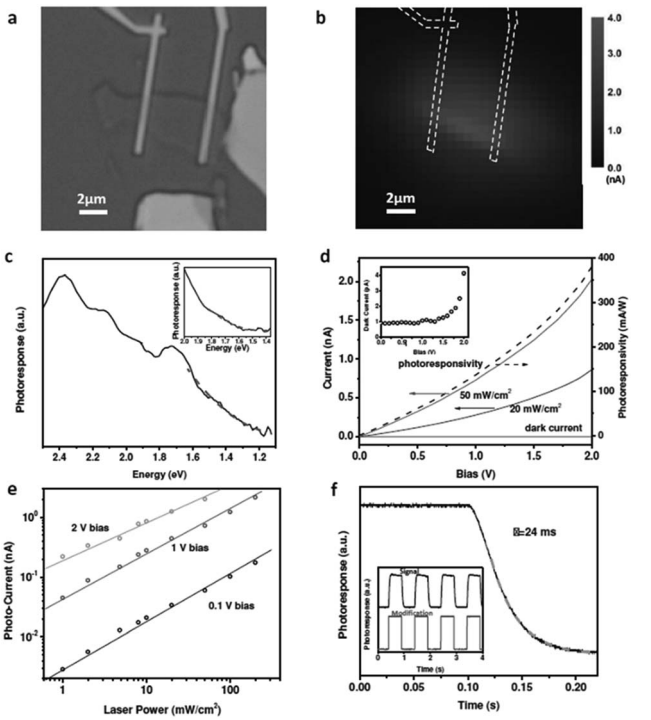

Fig. 22 Photoresponse study of mechanically exfoliated CIS few-layered samples. (a) Optical image of a 3–4 layered CIS flake photodetector. (b) The photocurrent mapping of the as-fabricated CIS photo-detector. (c) The photoconductivity spectrum of a 3–4 layered CIS sample with 2 μm electrode spacing indicates an indirect band-gap of 1.1 eV, while a 1–2 layered sample (inset) has a larger band gap of 1.4 eV. (d) Photoconductivity *IV* curves of the CIS photodetector. (e) The photoresponse is linear as a function of illumination intensity with a 0.1, 1, and 2 V bias. The illumination intensity ranges from 0 to 200 mW cm^{-2} and the current varies from 1 pA (dark current) to 2.16 nA, yielding a linear response range larger than 70 dB. (f) The time-resolved photoresponse measurement illustrates a stable photoresponse performance with a time constant of 24 ms. Reprinted from ref. 25 with permission from Wiley.

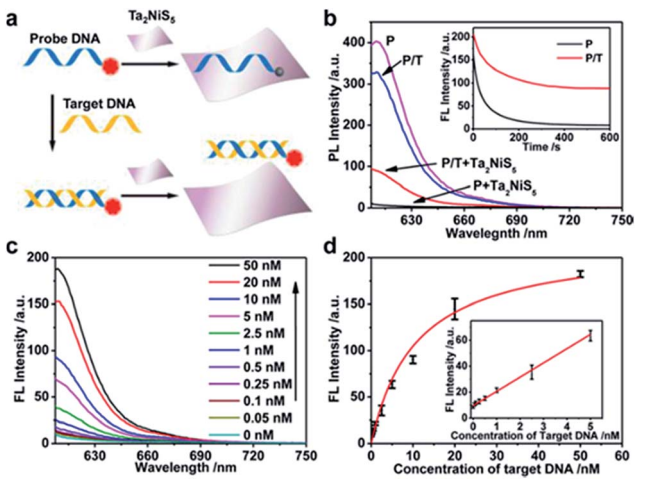

Fig. 23 Single-layer Ta_2NiS_5 nanosheet-based fluorescence sensor for DNA detection. (a) Schematic illustration of the DNA detection based on single-layer Ta_2NiS_5 nanosheets. (b) Fluorescence spectra of P (10 nM) and P/T (10 nM) in the absence and presence of single-layer Ta_2NiS_5 nanosheets. Inset: The fluorescence quenching curves of P and P/T in the presence of single-layer Ta_2NiS_5 nanosheets (4.0 μg mL^{-1}). (c) Fluorescence spectra of P in the presence of different concentrations of T (0, 0.05, 0.1, 0.25, 0.5, 1, 2.5, 5, 10, 20, and 50 nM) with addition of single-layer Ta_2NiS_5 nanosheets (4.0 μg mL^{-1}). (d) Calibration curve of DNA detection. Inset: The linear plot of the fluorescence peak intensity of P *vs.* the concentration of T with addition of single-layer Ta_2NiS_5 nanosheets (4.0 μg mL^{-1}). The excitation and emission wavelengths are 596 and 610 nm, respectively. Reprinted from ref. 23 with permission from the American Chemical Society.

could enable the fabrication of low-cost and efficient optoelectronic devices.

The fabrication of high-yield and large-scale ultrathin 2D ternary chalcogenide nanosheets in solution by exfoliation of their layered microflakes, including Ta_2NiS_5 and Ta_2NiSe_5, was reported.[23] Single-layer Ta_2NiS_5 nanosheets with a yield of approximately 86% were obtained. Due to their high fluorescence quenching ability, a novel fluorescent sensor for the detection of DNA was developed on the basis of single-layer Ta_2NiS_5 nanosheets. It showed excellent selectivity and sensitivity with a detection limit of 50 pM, which is better than that of the single-layer MoS_2-based biosensor (Fig. 23). This highly selective and sensitive biosensor might be used for real sample analysis in the near future.

5 Summary and outlook

This review summarizes recent work on various ternary 2D materials, including MTPs, ternary MXenes, ternary TMDs and other ternary 2D materials, regarding synthetic methods, structures, key properties (band gap tuning, phase transition and topological phase) and their potential applications. Ternary 2D systems provide additional degrees of freedom to tailor their band gap tuning and physical properties *via* stoichiometric engineering. As such, layered ternary 2D systems are an ideal platform for this line of research. However, to realize practical device applications, such as FETs, sensors and photodetectors, more effort is required to address the numerous issues related to the synthesis of materials. Technologies need to be developed to make high-quality layered ternary 2D materials with controlled layer numbers, size and homogeneity. In the present study, as described in the growth section, most ternary 2D materials are obtained by CVT and mechanical exfoliation methods. For instance, new ternary phase ZrSTe has been grown using the CVT technique, few-layered ReSSe and $PbSnS_2$ thin films are obtained by mechanical exfoliation from single crystals, and the most commonly adopted method of synthesizing MPTs is also realized by the CVT method. Given the advantage of the CVD method used in the binary 2D system, we may predict one promising direction in this field, *i.e.* CVD growth of high quality and large size few-layer ternary 2D crystals with controlled numbers. However, there are many challenges to produce single-layer and few-layer ternary 2D materials by the CVD method because the control of three elements is more difficult than binary ones. These need the efforts of more researchers. Meanwhile, approaches to control the composition of ternary 2D materials also need to be developed. For applications, for instance, studies on energy storage for ternary 2D materials are very limited. In this case, ternary MXenes show a striking ability to store Li^+/Na^+ and exhibit a superior specific capacity with improved stability compared to their binary systems. The distinctive properties of ternary MXene sheets make them promising candidates for electrode materials in LIBs and supercapacitors. Therefore, to further investigate the properties of ternary MXenes, it is imperative and indispensable to obtain single- or few-layers in the production by the exfoliation–intercalation method. As we reviewed above, ternary 2D systems are good candidates for investigating device applications (photodetectors, solar cells, sensors and FETs). Thus, it is important to fabricate high-performance devices using ternary 2D materials. Especially, ternary heterostructure devices have not been realized. They are expected to show high performance in photodetectors or other unique applications. In summary, for ternary 2D materials, the synthesis, potential applications, optical properties and fundamental physical properties all await further research efforts and increased understanding. We believe that ternary 2D materials are great candidates for application, and we hope more researchers will explore this area of materials and produce significant scientific developments.

Conflicts of interest

There are no conflicts to declare.

Acknowledgements

This work was financially supported by the National Natural Science Foundation of China (No. 51702203) and the Singapore National Research Foundation under NRF RF Award No. NRF-RF2013-08; MOE Tier 2 grant MOE2015-T2-2-007, MOE2016-T2-1-131, and MOE2016-T2-2-153.

Notes and references

1 K. S. Novoselov, A. K. Geim, S. V. Morozov, D. Jiang, Y. Zhang, S. V. Dubonos, I. V. Grigorieva and A. A. Firsov, *Science*, 2004, **306**, 666–669.
2 S. Bae, H. Kim, Y. Lee, X. F. Xu, J. S. Park, Y. Zheng, J. Balakrishnan, T. Lei, H. R. Kim, Y. I. Song, Y. J. Kim, K. S. Kim, B. Ozyilmaz, J. H. Ahn, B. H. Hong and S. Iijima, *Nat. Nanotechnol.*, 2010, **5**, 574–578.
3 M. C. Hu, Z. H. Yao and X. Q. Wang, *Ind. Eng. Chem. Res.*, 2017, **56**, 3477–3502.
4 F. Withers, T. H. Bointon, M. F. Craciun and S. Russo, *ACS Nano*, 2013, **7**, 5052–5057.
5 B.-M. Goh, Y. Wang, M. V. Reddy, Y. L. Ding, L. Lu, C. Bunker and K. P. Loh, *ACS Appl. Mater. Interfaces*, 2014, **6**, 9835–9841.
6 K. M. F. Shahil and A. A. Balandin, *Nano Lett.*, 2012, **12**, 861–867.
7 T. J. Echtermeyer, S. Milana, U. Sassi, A. Eiden, M. Wu, E. Lidorikis and A. C. Ferrari, *Nano Lett.*, 2016, **16**, 8–20.
8 J. Chen, Y. Wang, J. Cao, Y. Liu, Y. Zhou, J. H. Ouyang and D. Jia, *ACS Appl. Mater. Interfaces*, 2017, **9**, 19831–19842.
9 A. Subrati, S. Mondal, M. Ali, A. Alhindi, R. Ghazi, A. Abdala, D. Reinalda and S. Alhassan, *Ind. Eng. Chem. Res.*, 2017, **56**, 6945–6951.
10 L. Shi, C. Pang, S. Chen, M. Wang, K. Wang, Z. Tan, P. Gao, J. Ren, Y. Huang, H. Peng and Z. Liu, *Nano Lett.*, 2017, **17**, 3681–3687.
11 Y. Guo, G. Zhao, N. Wu, Y. Zhang, M. Xiang, B. Wang, H. Liu and H. Wu, *ACS Appl. Mater. Interfaces*, 2016, **8**, 34185–34193.

12 S. Balendhran, S. Walia, H. Nili, J. Z. Ou, S. Zhuiykov, R. B. Kaner, S. Sriram, M. Bhaskaran and K. Kalantar-zadeh, *Adv. Funct. Mater.*, 2013, **23**, 3952–3970.
13 M. Ghidiu, J. Halim, S. Kota, D. Bish, Y. Gogotsi and M. W. Barsoum, *Chem. Mater.*, 2016, **28**, 3507–3514.
14 H. Zhang, *ACS Nano*, 2015, **9**, 9451–9469.
15 X. Zhou, Q. Zhang, L. Gan, H. Li, J. Xiong and T. Zhai, *Adv. Sci.*, 2016, **3**, 1600177.
16 F. F. Cui, C. Wang, X. B. Li, G. Wang, K. Q. Liu, Z. Yang, Q. L. Feng, X. Liang, Z. Y. Zhang, S. Z. Liu, Z. B. Lei, Z. H. Liu, H. Xu and J. Zhang, *Adv. Mater.*, 2016, **28**, 5019–5024.
17 Z. Y. Dai, X. X. Zang, J. Yang, C. C. Sun, W. L. Si, W. Huang and X. C. Dong, *ACS Appl. Mater. Interfaces*, 2015, **7**, 25396–25401.
18 W. Fu, F. H. Du, J. Su, X. H. Li, X. Wei, T. N. Ye, K. X. Wang and J. S. Chen, *Sci. Rep.*, 2014, **4**, 4673.
19 T. Fujita, Y. Ito, Y. W. Tan, H. Yamaguchi, D. Hojo, A. Hirata, D. Voiry, M. Chhowalla and M. W. Chen, *Nanoscale*, 2014, **6**, 12458–12462.
20 V. Eswaraiah, Q. Zeng, Y. Long and Z. Liu, *Small*, 2016, **12**, 3480–3502.
21 L. Song, Z. Liu, A. L. M. Reddy, N. T. Narayanan, J. Taha-Tijerina, J. Peng, G. H. Gao, J. Lou, R. Vajtai and P. M. Ajayan, *Adv. Mater.*, 2012, **24**, 4878–4895.
22 L. Ci, L. Song, C. H. Jin, D. Jariwala, D. X. Wu, Y. J. Li, A. Srivastava, Z. F. Wang, K. Storr, L. Balicas, F. Liu and P. M. Ajayan, *Nat. Mater.*, 2010, **9**, 430–435.
23 C. L. Tan, P. Yu, Y. L. Hu, J. Z. Chen, Y. Huang, Y. Q. Cai, Z. M. Luo, B. Li, Q. P. Lu, L. H. Wang, Z. Liu and H. Zhang, *J. Am. Chem. Soc.*, 2015, **137**, 10430–10436.
24 J. Liu, H. Wang, C. Fang, L. Fu and X. Qian, *Nano Lett.*, 2017, **17**, 467–475.
25 S. D. Lei, A. Sobhani, F. F. Wen, A. George, Q. Z. Wang, Y. H. Huang, P. Dong, B. Li, S. Najmaei, J. Bellah, G. Gupta, A. D. Mohite, L. H. Ge, J. Lou, N. J. Halas, R. Vajtai and P. Ajayan, *Adv. Mater.*, 2014, **26**, 7666–7672.
26 M.-W. Lin, H. L. Zhuang, J. Yan, T. Z. Ward, A. A. Puretzky, C. M. Rouleau, Z. Gai, L. Liang, V. Meunier, B. G. Sumpter, P. Ganesh, P. R. C. Kent, D. B. Geohegan, D. G. Mandrus and K. Xiao, *J. Mater. Chem. C*, 2016, **4**, 315–322.
27 P. A. Hu, Z. Z. Wen, L. F. Wang, P. H. Tan and K. Xiao, *ACS Nano*, 2012, **6**, 5988–5994.
28 S. D. Lei, L. H. Ge, S. Najmaei, A. George, R. Kappera, J. Lou, M. Chhowalla, H. Yamaguchi, G. Gupta, R. Vajtai, A. D. Mohite and P. M. Ajayan, *ACS Nano*, 2014, **8**, 1263–1272.
29 P. G. Yan, H. Chen, J. D. Yin, Z. H. Xu, J. R. Li, Z. K. Jiang, W. F. Zhang, J. Z. Wang, I. L. Li, Z. P. Sun and S. C. Ruan, *Nanoscale*, 2017, **9**, 1871–1877.
30 X. Zhou, N. Zhou, C. Li, H. Y. Song, Q. Zhang, X. Z. Hu, L. Gan, H. Q. Li, J. T. Lu, J. Luo, J. Xiong and T. Y. Zhai, *2D Mater.*, 2017, **4**, 025048.
31 O. Lopez-Sanchez, D. Lembke, M. Kayci, A. Radenovic and A. Kis, *Nat. Nanotechnol.*, 2013, **8**, 497–501.
32 R. B. Jacobs-Gedrim, M. Shanmugam, N. Jain, C. A. Durcan, M. T. Murphy, T. M. Murray, R. J. Matyi, R. L. Moore and B. Yu, *ACS Nano*, 2014, **8**, 514–521.
33 S. R. Tamalampudi, Y. Y. Lu, U. R. Kumar, R. Sankar, C. D. Liao, B. K. Moorthy, C. H. Cheng, F. C. Chou and Y. T. Chen, *Nano Lett.*, 2014, **14**, 2800–2806.
34 T. Maeda, W. Y. Gong and T. Wada, *Jpn. J. Appl. Phys.*, 2016, **55**, 04ES15.
35 B. Siberchicot, S. Jobic, V. Carteaux, P. Gressier and G. Ouvrard, *J. Phys. Chem.*, 1996, **100**, 5863–5867.
36 L. Britnell, R. M. Ribeiro, A. Eckmann, R. Jalil, B. D. Belle, A. Mishchenko, Y. J. Kim, R. V. Gorbachev, T. Georgiou, S. V. Morozov, A. N. Grigorenko, A. K. Geim, C. Casiraghi, A. H. Castro Neto and K. S. Novoselov, *Science*, 2013, **340**, 1311–1314.
37 B. L. Chittari, Y. Park, D. Lee, M. Han, A. H. MacDonald, E. Hwang and J. Jung, *Phys. Rev. B: Condens. Matter Mater. Phys.*, 2016, **94**, 184428.
38 A. H. Castro Neto, *Phys. Rev. Lett.*, 2001, **86**, 4382–4385.
39 D. Costanzo, S. Jo, H. Berger and A. F. Morpurgo, *Nat. Nanotechnol.*, 2016, **11**, 339–344.
40 R. F. Frindt, *Phys. Rev. Lett.*, 1972, **28**, 299–301.
41 Y. Ma, Y. Dai, M. Guo, C. Niu, Y. Zhu and B. Huang, *ACS Nano*, 2012, **6**, 1695–1701.
42 S. Lebègue, T. Björkman, M. Klintenberg, R. M. Nieminen and O. Eriksson, *Phys. Rev. X*, 2013, **3**, 031002.
43 J. Liu, S. Y. Park, K. F. Garrity and D. Vanderbilt, *Phys. Rev. Lett.*, 2016, **117**, 257201.
44 M. Zybert, M. Marchewka, E. M. Sheregii, D. G. Rickel, J. B. Betts, F. F. Balakirev, M. Gordon, A. V. Stier, C. H. Mielke, P. Pfeffer and W. Zawadzki, *Phys. Rev. B: Condens. Matter Mater. Phys.*, 2017, **95**, 115432.
45 H. L. Zhuang, Y. Xie, P. R. C. Kent and P. Ganesh, *Phys. Rev. B: Condens. Matter Mater. Phys.*, 2015, **92**, 035407.
46 Y. Fukuma, H. Asada, S. Senba and T. Koyanagi, *Appl. Phys. Lett.*, 2016, **108**, 222403.
47 Q. S. Zeng, H. Wang, W. Fu, Y. J. Gong, W. Zhou, P. M. Ajayan, J. Lou and Z. Liu, *Small*, 2015, **11**, 1868–1884.
48 T. A. Shifa, F. M. Wang, K. L. Liu, K. Xu, Z. X. Wang, X. Y. Zhan, C. Jiang and J. He, *Small*, 2016, **12**, 3802–3809.
49 Y. J. Gong, Z. Liu, A. R. Lupini, G. Shi, J. H. Lin, S. Najmaei, Z. Lin, A. L. Elias, A. Berkdemir, G. You, H. Terrones, M. Terrones, R. Vajtai, S. T. Pantelides, S. J. Pennycook, J. Lou, W. Zhou and P. M. Ajayan, *Nano Lett.*, 2014, **14**, 442–449.
50 J. F. Shen, J. Ji, P. Dong, R. Baines, Z. Q. Zhang, P. M. Ajayan and M. X. Ye, *J. Mater. Chem. A*, 2016, **4**, 8844–8850.
51 W. T. Zhang, X. D. Li, T. T. Jiang, J. L. Q. Song, Y. Lin, L. X. Zhu and X. L. Xu, *Nanoscale*, 2015, **7**, 13554–13560.
52 S. J. Zheng, L. F. Sun, T. T. Yin, A. M. Dubrovkin, F. C. Liu, Z. Liu, Z. X. Shen and H. J. Fan, *Appl. Phys. Lett.*, 2015, **106**, 063113.
53 S. D. Karande, N. Kaushik, D. S. Narang, D. Late and S. Lodha, *Appl. Phys. Lett.*, 2016, **109**, 142101.
54 B. Konkena, J. Masa, W. Xia, M. Muhler and W. Schuhmann, *Nano Energy*, 2016, **29**, 46–53.

55 M. Moustafa, A. Paulheim, M. Mohamed, C. Janowitz and R. Manzke, *Appl. Surf. Sci.*, 2016, **366**, 397–403.
56 A. K. Dasadia, B. B. Nariya and A. R. Jani, *J. Cryst. Growth*, 2015, **426**, 265–269.
57 A. Łapinska, A. Taube, M. Wasik, G. Z. Zukowska, A. Duzynska, J. Judek and M. Zdrojek, *J. Raman Spectrosc.*, 2017, **48**, 479–484.
58 P. Yu, J. H. Lin, L. F. Sun, Q. L. Le, X. C. Yu, G. H. Gao, C. H. Hsu, D. Wu, T. R. Chang, Q. S. Zeng, F. C. Liu, Q. J. Wang, H. T. Jeng, H. Lin, A. Trampert, Z. X. Shen, K. Suenaga and Z. Liu, *Adv. Mater.*, 2017, **29**, 1603991.
59 K. Z. Du, X. Z. Wang, Y. Liu, P. Hu, M. I. B. Utama, C. K. Gan, Q. H. Xiong and C. Kloc, *ACS Nano*, 2016, **10**, 1738–1743.
60 A. Villanueva, M. C. Morales-Varela and E. Ruiz-Hitzky, *Eur. J. Inorg. Chem.*, 2004, **2004**, 949–952.
61 J. D. Yao, Z. Q. Zheng and G. W. Yang, *ACS Appl. Mater. Interfaces*, 2016, **8**, 12915–12924.
62 V. Kiran, D. Mukherjee, R. N. Jenjeti and S. Sampath, *Nanoscale*, 2014, **6**, 12856–12863.
63 J. F. Shen, P. Dong, R. Baines, X. W. Xu, Z. Q. Zhang, P. M. Ajayan and M. X. Ye, *Chem. Commun.*, 2016, **52**, 9251–9254.
64 J. U. Lee, S. Lee, J. H. Ryoo, S. Kang, T. Y. Kim, P. Kim, C. H. Park, J. G. Park and H. Cheong, *Nano Lett.*, 2016, **16**, 7433–7438.
65 X. Wang, K. Du, Y. Y. F. Liu, P. Hu, J. Zhang, Q. Zhang, M. H. S. Owen, X. Lu, C. K. Gan and P. Sengupta, *2D Mater.*, 2016, **3**, 031009.
66 W. Toyoshima, T. Masubuchi, T. Watanabe, K. Takase, K. Matsubayashi, Y. Uwatoko and Y. Takano, *J. Phys.: Conf. Ser.*, 2009, **150**, 042215.
67 C. C. Mayorga-Martinez, Z. Sofer, D. Sedmidubsky, S. Huber, A. Y. S. Eng and M. Pumera, *ACS Appl. Mater. Interfaces*, 2017, **9**, 12563–12573.
68 N. Ismail, A. A. El-Meligi, Y. M. Temerk and M. Madian, *Int. J. Hydrogen Energy*, 2010, **35**, 7827–7834.
69 N. Ismail, Y. M. Temerk, A. A. El-Meligi, M. A. Badr and M. Madian, *J. Solid State Chem.*, 2010, **183**, 984–987.
70 D. Mukherjee, P. M. Austeria and S. Sampath, *ACS Energy Lett.*, 2016, **1**, 367–372.
71 Y. Gogotsi, *Nat. Mater.*, 2015, **14**, 1079–1080.
72 M. Naguib, M. Kurtoglu, V. Presser, J. Lu, J. J. Niu, M. Heon, L. Hultman, Y. Gogotsi and M. W. Barsoum, *Adv. Mater.*, 2011, **23**, 4248–4253.
73 O. Mashtalir, M. R. Lukatskaya, M. Q. Zhao, M. W. Barsoum and Y. Gogotsi, *Adv. Mater.*, 2015, **27**, 3501–3506.
74 R. Zeng, S. Q. Wang, G. D. Du, J. L. Wang, J. C. Debnath, P. Shamba, Z. Y. Fang and S. X. Dou, *J. Appl. Phys.*, 2012, **111**, 07E144.
75 H. Falius, *Z. Anorg. Allg. Chem.*, 1968, **356**, 189–194.
76 O. Mashtalir, M. Naguib, B. Dyatkin, Y. Gogotsi and M. W. Barsoum, *Mater. Chem. Phys.*, 2013, **139**, 147–152.
77 M. Naguib, V. N. Mochalin, M. W. Barsoum and Y. Gogotsi, *Adv. Mater.*, 2014, **26**, 992–1005.
78 B. Anasori, M. R. Lukatskaya and Y. Gogotsi, *Nat. Rev. Mater.*, 2017, **2**, 16098.
79 M. Naguib, O. Mashtalir, J. Carle, V. Presser, J. Lu, L. Hultman, Y. Gogotsi and M. W. Barsoum, *ACS Nano*, 2012, **6**, 1322–1331.
80 B. Chen, F. Chang, J. Yang, H. Tang and C. Li, *Cryst. Res. Technol.*, 2014, **49**, 813–819.
81 L. Liu, J. Park, D. A. Siegel, K. F. McCarty, K. W. Clark, W. Deng, L. Basile, J. C. Idrobo, A. P. Li and G. Gu, *Science*, 2014, **343**, 163–167.
82 F. K. Ma, M. X. Wang, Y. L. Shao, L. J. Wang, Y. Z. Wu, Z. P. Wang and X. P. Hao, *J. Mater. Chem. C*, 2017, **5**, 2559–2565.
83 M. Ghidiu, M. R. Lukatskaya, M.-Q. Zhao, Y. Gogotsi and M. W. Barsoum, *Nature*, 2014, **516**, 78–81.
84 J. Halim, S. Kota, M. R. Lukatskaya, M. Naguib, M. Q. Zhao, E. J. Moon, J. Pitock, J. Nanda, S. J. May and Y. Gogotsi, *Adv. Funct. Mater.*, 2016, **26**, 3118.
85 Z. W. Seh, K. D. Fredrickson, B. Anasori, J. Kibsgaard, A. L. Strickler, M. R. Lukatskaya, Y. Gogotsi, T. F. Jaramillo and A. Vojvodic, *ACS Energy Lett.*, 2016, **1**, 589–594.
86 A. Lipatov, M. Alhabeb, M. R. Lukatskaya, A. Boson, Y. Gogotsi and A. Sinitskii, *Adv. Electron. Mater.*, 2016, **2**, 1600255.
87 O. Mashtalir, M. Naguib, V. N. Mochalin, Y. Dall'Agnese, M. Heon, M. W. Barsoum and Y. Gogotsi, *Nat. Commun.*, 2013, **4**, 1716.
88 M. Naguib, R. R. Unocic, B. L. Armstrong and J. Nanda, *Dalton Trans.*, 2015, **44**, 9353–9358.
89 Y. Gogotsi, *Nat. Mater.*, 2015, **14**, 1079–1080.
90 Y. Miyamoto, A. Rubio, M. L. Cohen and S. G. Louie, *Phys. Rev. B: Condens. Matter Mater. Phys.*, 1994, **50**, 4976.
91 A. Rubio, J. L. Corkill and M. L. Cohen, *Phys. Rev. B: Condens. Matter Mater. Phys.*, 1994, **49**, 5081.
92 Z. Liu, L. L. Ma, G. Shi, W. Zhou, Y. J. Gong, S. D. Lei, X. B. Yang, J. N. Zhang, J. J. Yu, K. P. Hackenberg, A. Babakhani, J. C. Idrobo, R. Vajtai, J. Lou and P. M. Ajayan, *Nat. Nanotechnol.*, 2013, **8**, 119–124.
93 J. T. Jin, F. P. Pan, L. H. Jiang, X. G. Fu, A. M. Liang, Z. Y. Wei, J. Y. Zhang and G. Q. Sun, *ACS Nano*, 2014, **8**, 3313–3321.
94 Y. J. Gong, G. Shi, Z. H. Zhang, W. Zhou, J. Jung, W. L. Gao, L. L. Ma, Y. Yang, S. B. Yang, G. You, R. Vajtai, Q. F. Xu, A. H. MacDonald, B. I. Yakobson, J. Lou, Z. Liu and P. M. Ajayan, *Nat. Commun.*, 2014, **5**, 3193.
95 S. Zhang, J. Wu, Q. Yang, R. Tu, C. B. Wang, Q. Shen and L. M. Zhang, *AIP Adv.*, 2015, **5**, 047125.
96 C. J. Huang, C. Chen, M. W. Zhang, L. H. Lin, X. X. Ye, S. Lin, M. Antonietti and X. C. Wang, *Nat. Commun.*, 2015, **6**, 7698.
97 S. F. Zeng, W. L. Feng, H. Luo, Y. Q. Tan, Y. Wang, H. B. Zhang, T. Zhang and S. M. Peng, *Chem. Phys. Lett.*, 2017, **674**, 164–167.
98 T. Zhang, S. Zeng and G. Wen, *Mater. Lett.*, 2014, **132**, 277–280.
99 L. Massimi, M. G. Betti, S. Caramazza, P. Postorino, C. Mariani, A. Latini and F. Leardini, *Nanotechnology*, 2016, **27**, 435601.

100 Z. Han, G. Li, J. Tian and M. Gu, *Mater. Lett.*, 2002, **57**, 899–903.
101 X. R. Deng, H. Kousaka, T. Tokoroyama and N. Umehara, *Surf. Coat. Technol.*, 2014, **259**, 2–6.
102 Y. Chen, J. Xi, D. O. Dumcenco, Z. Liu, K. Suenaga, D. Wang, Z. Shuai, Y.-S. Huang and L. Xie, *ACS Nano*, 2013, **7**, 4610–4616.
103 C. Tan, W. Zhao, A. Chaturvedi, Z. Fei, Z. Zeng, J. Chen, Y. Huang, P. Ercius, Z. Luo, X. Qi, B. Chen, Z. Lai, B. Li, X. Zhang, J. Yang, Y. Zong, C. Jin, H. Zheng, C. Kloc and H. Zhang, *Small*, 2016, **12**, 1866–1874.
104 T. Tavsanoglu, M. Jeandin and O. Addemir, *Surf. Eng.*, 2016, **32**, 755–760.
105 S. Beniwal, J. Hooper, D. P. Miller, P. S. Costa, G. Chen, S. Y. Liu, P. A. Dowben, E. C. H. Sykes, E. Zurek and A. Enders, *ACS Nano*, 2017, **11**, 2486–2493.
106 J. Wu, H. Yuan, M. Meng, C. Chen, Y. Sun, Z. Chen, W. Dang, C. Tan, Y. Liu, J. Yin, Y. Zhou, S. Huang, H. Q. Xu, Y. Cui, H. Y. Hwang, Z. Liu, Y. Chen, B. Yan and H. Peng, *Nat. Nanotechnol.*, 2017, **12**, 530–534.
107 Y. Shi, H. Li and L.-J. Li, *Chem. Soc. Rev.*, 2015, **44**, 2744–2756.
108 Q. Gong, L. Cheng, C. Liu, M. Zhang, Q. Feng, H. Ye, M. Zeng, L. Xie, Z. Liu and Y. Li, *ACS Catal.*, 2015, **5**, 2213–2219.
109 F. Liu, S. Zheng, A. Chaturvedi, V. Zolyomi, J. Zhou, Q. Fu, C. Zhu, P. Yu, Q. Zeng, N. D. Drummond, H. J. Fan, C. Kloc, V. I. Fal'ko, X. He and Z. Liu, *Nanoscale*, 2016, **8**, 5826–5834.
110 J. Xi, T. Zhao, D. Wang and Z. Shuai, *J. Phys. Chem. Lett.*, 2014, **5**, 285–291.
111 H. Li, X. Duan, X. Wu, X. Zhuang, H. Zhou, Q. Zhang, X. Zhu, W. Hu, P. Ren, P. Guo, L. Ma, X. Fan, X. Wang, J. Xu, A. Pan and X. Duan, *J. Am. Chem. Soc.*, 2014, **136**, 3756–3759.
112 Q. Feng, Y. Zhu, J. Hong, M. Zhang, W. Duan, N. Mao, J. Wu, H. Xu, F. Dong, F. Lin, C. Jin, C. Wang, J. Zhang and L. Xie, *Adv. Mater.*, 2014, **26**, 2648–2653.
113 H. Weyl, *Z. Phys.*, 1929, **56**, 330–352.
114 L. Huang, T. M. McCormick, M. Ochi, Z. Zhao, M.-T. Suzuki, R. Arita, Y. Wu, D. Mou, H. Cao, J. Yan, N. Trivedi and A. Kaminski, *Nat. Mater.*, 2016, **15**, 1155–1160.
115 I. Belopolski, S. Y. Xu, Y. Ishida, X. C. Pan, P. Yu, D. S. Sanchez, H. Zheng, M. Neupane, N. Alidoust, G. Q. Chang, T. R. Chang, Y. Wu, G. Bian, S. M. Huang, C. C. Lee, D. X. Mou, L. N. Huang, Y. Song, B. G. Wang, G. H. Wang, Y. W. Yeh, N. Yao, J. E. Rault, P. Le Fevre, F. Bertran, H. T. Jeng, T. Kondo, A. Kaminski, H. Lin, Z. Liu, F. Q. Song, S. Shin and M. Z. Hasan, *Phys. Rev. B: Condens. Matter Mater. Phys.*, 2016, **94**, 085127.
116 A. A. Soluyanov, D. Gresch, Z. Wang, Q. Wu, M. Troyer, X. Dai and B. A. Bernevig, *Nature*, 2015, **527**, 495–498.
117 G. Autès, D. Gresch, M. Troyer, A. A. Soluyanov and O. V. Yazyev, *Phys. Rev. Lett.*, 2016, **117**, 066402.
118 K. Koepernik, D. Kasinathan, D. V. Efremov, S. Khim, S. Borisenko, B. Buchner and J. van den Brink, *Phys. Rev. B: Condens. Matter Mater. Phys.*, 2016, **93**, 201101(R).
119 R. Brec, D. M. Schleich, G. Ouvrard, A. Louisy and J. Rouxel, *Inorg. Chem.*, 1979, **18**, 1814–1818.
120 V. Nicolosi, M. Chhowalla, M. G. Kanatzidis, M. S. Strano and J. N. Coleman, *Science*, 2013, **340**, 1226419.
121 R. Brec, *Solid State Ionics*, 1986, **22**, 3–30.
122 J. Liu, X.-B. Li, D. Wang, W.-M. Lau, P. Peng and L.-M. Liu, *J. Chem. Phys.*, 2014, **140**, 054707.
123 H. Xiang, B. Xu, Y. Xia, J. Yin and Z. Liu, *RSC Adv.*, 2016, **6**, 89901–89906.
124 C. Sourisseau, J. P. Forgerit and Y. Mathey, *J. Solid State Chem.*, 1983, **49**, 134–149.
125 M. Scagliotti, M. Jouanne, M. Balkanski, G. Ouvrard and G. Benedek, *Phys. Rev. B: Condens. Matter Mater. Phys.*, 1987, **35**, 7097–7104.
126 P. Jernberg, S. Bjarman and R. Wäppling, *J. Magn. Magn. Mater.*, 1984, **46**, 178–190.
127 M. Khazaei, A. Ranjbar, M. Arai, T. Sasaki and S. Yunoki, *J. Mater. Chem. C*, 2017, **5**, 2488–2503.
128 V. M. Hong Ng, H. Huang, K. Zhou, P. S. Lee, W. Que, J. Z. Xu and L. B. Kong, *J. Mater. Chem. A*, 2017, **5**, 3039–3068.
129 M. Naguib, J. Halim, J. Lu, K. M. Cook, L. Hultman, Y. Gogotsi and M. W. Barsoum, *J. Am. Chem. Soc.*, 2013, **135**, 15966–15969.
130 B. Anasori, Y. Xie, M. Beidaghi, J. Lu, B. C. Hosler, L. Hultman, P. R. C. Kent, Y. Gogotsi and M. W. Barsoum, *ACS Nano*, 2015, **9**, 9507–9516.
131 M. Khazaei, A. Ranjbar, M. Arai and S. Yunoki, *Phys. Rev. B: Condens. Matter Mater. Phys.*, 2016, **94**, 125152.
132 R. Meshkian, Q. Tao, M. Dahlqvist, J. Lu, L. Hultman and J. Rosen, *Acta Mater.*, 2017, **125**, 476–480.
133 O. Stephan, P. M. Ajayan, C. Colliex, P. Redlich, J. M. Lambert, P. Bernier and P. Lefin, *Science*, 1994, **266**, 1683–1685.
134 J. Wu, H. Yuan, M. Meng, C. Chen, Y. Sun, Z. Chen, W. Dang, C. Tan, Y. Liu and J. Yin, *Nat. Nanotechnol.*, 2017, **12**, 530.
135 C. Gong, L. Li, Z. L. Li, H. W. Ji, A. Stern, Y. Xia, T. Cao, W. Bao, C. Z. Wang, Y. A. Wang, Z. Q. Qiu, R. J. Cava, S. G. Louie, J. Xia and X. Zhang, *Nature*, 2017, **546**, 265–269.
136 H. Pan, *J. Mater. Chem. A*, 2015, **3**, 21486–21493.
137 Y. Y. Peng, B. Akuzum, N. Kurra, M. Q. Zhao, M. Alhabe, B. Anasori, E. C. Kumbur, H. N. Alshareef, M. D. Ger and Y. Gogotsi, *Energy Environ. Sci.*, 2016, **9**, 2847–2854.
138 Q. Fu, J. Wen, N. Zhang, L. Wu, M. Zhang, S. Lin, H. Gao and X. Zhang, *RSC Adv.*, 2017, **7**, 11998–12005.
139 O. Mashtalir, M. Naguib, V. N. Mochalin, Y. Dall'Agnese, M. Heon, M. W. Barsoum and Y. Gogotsi, *Nat. Commun.*, 2013, **4**, 1716.
140 C. Eames and M. S. Islam, *J. Am. Chem. Soc.*, 2014, **136**, 16270–16276.
141 P. Kumar, H. Abuhimd, W. Wahyudi, M. L. Li, J. Ming and L. J. Li, *ECS J. Solid State Sci. Technol.*, 2016, **5**, Q3021–Q3025.
142 J. Yang, M. Naguib, M. Ghidiu, L. M. Pan, J. Gu, J. Nanda, J. Halim, Y. Gogotsi and M. W. Barsoum, *J. Am. Ceram. Soc.*, 2016, **99**, 660–666.

143 A. H. Thompson and M. S. Whittingham, *Mater. Res. Bull.*, 1977, **12**, 741–744.
144 Y. V. Kuz'minskii, B. M. Voronin, I. M. Petrushina, N. N. Redin and G. P. Prikhodko, *J. Power Sources*, 1995, **55**, 1–6.
145 X. Peng, L. Peng, C. Wu and Y. Xie, *Chem. Soc. Rev.*, 2014, **43**, 3303–3323.
146 N. Choudhary, C. Li, H.-S. Chung, J. Moore, J. Thomas and Y. Jung, *ACS Nano*, 2016, **10**, 10726–10735.
147 J. Zhou, J. Qin, L. Guo, N. Zhao, C. Shi, E.-z. Liu, F. He, L. Ma, J. Li and C. He, *J. Mater. Chem. A*, 2016, **4**, 17370–17380.
148 S. Zhang, Z. Huang, Z. Wen, L. Zhang, J. Jin, R. Shahbazian-Yassar and J. Yang, *Nano Lett.*, 2017, **17**, 3518–3526.
149 P. C. K. Vesborg, B. Seger and I. Chorkendorff, *J. Phys. Chem. Lett.*, 2015, **6**, 951–957.
150 P. C. K. Vesborg and T. F. Jaramillo, *RSC Adv.*, 2012, **2**, 7933–7947.
151 K. C. Neyerlin, W. Gu, J. Jorne and H. A. Gasteiger, *J. Electrochem. Soc.*, 2007, **154**, B631–B635.
152 M. Zeng and Y. Li, *J. Mater. Chem. A*, 2015, **3**, 14942–14962.
153 H. Wang, R. Peng, Z. D. Hood, M. Naguib, S. P. Adhikari and Z. Wu, *ChemSusChem*, 2016, **9**, 1490–1497.
154 Z. Guo, J. Zhou, L. Zhu and Z. Sun, *J. Mater. Chem. A*, 2016, **4**, 11446–11452.
155 T. Y. Ma, J. L. Cao, M. Jaroniec and S. Z. Qiao, *Angew. Chem., Int. Ed.*, 2016, **55**, 1138–1142.
156 K. Xu, F. Wang, Z. Wang, X. Zhan, Q. Wang, Z. Cheng, M. Safdar and J. He, *ACS Nano*, 2014, **8**, 8468–8476.
157 K. Liu, F. Wang, K. Xu, T. A. Shifa, Z. Cheng, X. Zhan and J. He, *Nanoscale*, 2016, **8**, 4699–4704.
158 B. Hinnemann, P. G. Moses, J. Bonde, K. P. Jørgensen, J. H. Nielsen, S. Horch, I. Chorkendorff and J. K. Nørskov, *J. Am. Chem. Soc.*, 2005, **127**, 5308–5309.
159 T. F. Jaramillo, K. P. Jørgensen, J. Bonde, J. H. Nielsen, S. Horch and I. Chorkendorff, *Science*, 2007, **317**, 100–102.
160 J. Yang and H. S. Shin, *J. Mater. Chem. A*, 2014, **2**, 5979–5985.
161 D. Kong, J. J. Cha, H. Wang, H. R. Lee and Y. Cui, *Energy Environ. Sci.*, 2013, **6**, 3553–3558.
162 H. Tang, K. Dou, C.-C. Kaun, Q. Kuang and S. Yang, *J. Mater. Chem. A*, 2014, **2**, 360–364.
163 D. Voiry, H. Yamaguchi, J. Li, R. Silva, D. C. B. Alves, T. Fujita, M. Chen, T. Asefa, V. B. Shenoy, G. Eda and M. Chhowalla, *Nat. Mater.*, 2013, **12**, 850–855.
164 J. Lin, Z. Peng, G. Wang, D. Zakhidov, E. Larios, M. J. Yacaman and J. M. Tour, *Adv. Energy Mater.*, 2014, **4**, 1301875.
165 J. Xie, J. Zhang, S. Li, F. Grote, X. Zhang, H. Zhang, R. Wang, Y. Lei, B. Pan and Y. Xie, *J. Am. Chem. Soc.*, 2013, **135**, 17881–17888.